Helically coiled solar cavity receiver for micro-scale direct steam generation

Jonathan K. Swanepoel, Willem G. le Roux*, Axel S. Lexmond and Josua P. Meyer

Department of Mechanical and Aeronautical Engineering, University of Pretoria,

Private Bag X20, Hatfield, 0028, South Africa

*Corresponding author: willem.leroux@up.ac.za

Highlights

- Naturalistic, micro-scale direct steam generation using a solar dish is considered.
- A helically coiled cavity receiver and a novel multifaceted solar dish are used.
- Energy and exergy analysis of the helically coiled cavity receiver is presented.
- Collector and receiver efficiencies of 42% and 50% were found, respectively.
- Flow patterns inside the receiver coil were investigated.

Abstract

Concentrated solar systems have a large potential for power generation and water pumping in rural off-grid settlements with a high solar irradiance resource. With the use of a solar dish concentrator, superheated steam can be directly generated in a solar cavity receiver. Volumetric expanders show promise for micro-scale power production (below 1 kW). However, naturalistic experimental investigations of micro-scale direct steam generation using a solar dish is limited. In this work, a low-cost helically coiled cavity receiver and a novel solar concentrator manufactured from off-the-shelf components are experimentally investigated for steam generation at water pressures of above 3 bar. Working fluid temperatures were measured throughout the coil length and pressures were measured at the inlet and outlet of the receiver coil. Using a concentrator with a total incident area of 2.70 m^2 and a water flow rate of 0.294 g/s, the working fluid captured 861 W of heat with an outlet temperature of 343 °C at an average solar irradiance of 757 W/m^2. The average thermal

efficiencies of the collector and receiver were determined to be 42% and 50%, respectively, for the testing period. Furthermore, the average second-law efficiency was 12%. Flow patterns within the coil were investigated by considering the temperature differences between the coil surface and the working fluid. A heat loss model was developed that could predict the steady-state heat loss rate with an accuracy of 97%. The observations made during the study and the results obtained highlight important design aspects that need to be considered in future work.

Keywords: Steam generation; Solar thermal; Dish concentrator; Cavity receiver; Rankine.

1. Introduction

The supply of power to rural areas plays an important role in nearly all aspects of a population's welfare. When municipal electricity does not reach these areas or the municipal electricity rates are simply unaffordable, communities need to consider alternatives. Fossil fuels are considered a common solution. Kerosene lamps are used for lighting, biomass is used for heating and cooking, while fuel generators are used to provide critical electricity and power supply [1]. Distributed scale renewable power generation alternatives possess several advantages over current methods. One prominent advantage pertains to health benefits when substituting fuel-burning processes in the household with renewable alternatives. In Africa, the provision of adequate power to households negates the need for indoor kerosene lamps and biomass cooking, which emit harmful by-products, such as carbon monoxide, nitric oxide and sulphur dioxide, that lead to lung disease [2, 3]. The replacement of fuel generators with renewable solutions would not only aid in the sustainable development of the region but it could also potentially decrease the cost of power by harnessing local industrial and environmental resources to do so.

Micro-scale solar power generation is a renewable energy solution that has seen rapid growth in popularity in the past few years. There are currently two main ways of harnessing solar power. The prominent method is the use of photovoltaic (PV) panels, which converts light directly into electrical potential through the photoelectric effect [4]. The second method is to capture the solar irradiance in the form of heat using solar thermal generation methods. Solar PV solutions currently outperform solar thermal solutions with regard to solar-electrical

conversion efficiencies. Current commercial solar PV solutions have an electrical efficiency of 21% with more experimental PV solutions being able to reach 39% [5]. Small-scale solar thermal solutions have electrical conversion efficiencies ranging from 2% to 29%, depending on the type and size of the solar thermal power plant [6]. However, when considering the fact that some processes require direct mechanical work input or direct heat input, solar thermal solutions can begin competing with PV. Solar thermal generation has the ability to generate direct mechanical work output through the use of an expander as well as simultaneous process heating by capturing the runoff heat from the cycle. This mechanical work can be used in mechanical pumping processes and the process heat can be used in heating and cooling applications, which can be useful when considering power usage in rural areas.

In the early 2000s, Wong and Sumathy [7] reviewed both conventional and unconventional methods of solar pumping systems. The work concluded that solar thermal pumping solutions are more economical than electrical water pumps when considering fossil fuels, energy conversion, electricity transmission and system maintenance. Ali [8] performed a comparative feasibility study on possible methods for solar irrigation pumps to be implemented in agriculture in Sudan. This study compared the conventional methods of concentrated solar thermal and solar PV power generation. It was determined that concentrated solar systems, particularly the solar-dish water pumping systems, had a conversion efficiency of 22%, which was roughly 6.5 times more efficient than a solar PV system, which had a conversion efficiency of 3.4%. However, for Sudan, the normalised energy cost of solar PV power generation in $/kWh outperformed concentrated solar by a factor of 2. Mohammed Wazed et al. [9] presented a review of solar irrigation systems and discussed their viability in the context of rural sub-Saharan Africa. The study noted that one of the main drawbacks of a solar PV system was the large carbon footprint currently associated with the construction and importation of associated parts for solar PV systems into Africa since there is a lack of available, local manufacturing facilities. It was also noted that concentrated solar thermal systems have the potential to power irrigation systems in small-scale rural farming settlements in the region, but little research is available on the feasibility of implementing such methods.

Micro-scale power generation through direct steam generation faces challenges such as solar intermittency, lack in development of the adequate scale of expander technologies and the

steep start-up costs primarily associated with the collector. Thermal energy storage (TES) solutions may be used to accommodate solar intermittency by storing the thermal energy into materials that are generally cheaper, locally available and environmentally friendly. In comparison, solar PV solutions require advanced current regulation and battery technologies to store the captured electrical power which further impacts the solution's feasibility in powering rural areas. Alva et al. [10] present an overview of current methods of TES and the associated technology and materials. The study noted that TES does not undergo cycling-induced degradation as rapidly as PV and battery technologies do. Expander technology is currently being developed and optimised for micro-scale power generation [11-13]. Scroll expanders show particular potential to harness power at low steam mass flow rates but design challenges such as frictional losses, temperature limits and leakages need to be further developed [14].

Research on micro-scale solar thermal power generation currently lacks naturalistic experimental detail. Pavlovic et al. [15] performed a set of experiments on a simple, low-cost parabolic dish collector with a corrugated spiral absorber using water at operating temperatures below boiling temperature. Other current works on the research of micro-scale Rankine cycles are generally directed towards organic Rankine cycles for the use of waste heat recovery or low-temperature solar thermal power generation [16-18]. The work of Loni et al. [19] focused on the experimental analysis of small-scale, concentrated solar thermal organic Rankine cycles for indirect steam generation using a parabolic dish. The outlet temperatures of the heat transfer fluid from the receiver cavities ranged between 92 and 117 °C. Numerical models, characterising the performance of the receiver, were also validated against experimental results [20, 21]. Organic Rankine cycle power generation takes advantage of low-temperature evaporation (80 to 250 °C). Dry fluids are considered as the working fluids of organic Rankine cycles which are generally harmful to the environment and cannot easily be sourced in rural areas. However, water is available in most areas making it an attractive option for use in solar cavity receivers for steam generation.

Two-phase flow within vertically orientated helical coils has been experimentally investigated in lab settings. The work of Dean [22] initially investigated secondary flow in curved tubes and formulated a relationship between centrifugal forces and the inertial forces that a fluid would experience moving through the curved tube. Secondary flow in coiled tubes was investigated

by Ishida [23] and showed that centrifugal forces dominate the flow at high pressures while secondary forces dominate the flow at low pressure. Cui et al. [24] investigated flow patterns that would occur for flow boiling within micro-finned helically coiled tubes. Flow regimes for air-water flow were investigated by Zhu et al. [25] which showed that bubbly, plug and slug flow would be the first three flow regimes to occur in two-phase flow in a coiled tube. Based on these studies, it is noted that flow within helically coiled tubes is strongly dependant on the coil dimensions, the operating conditions and the working fluid selected.

Boiling flow through helical coils is underdefined in current literature, particularly concerning flow patterns occurring under non-uniform incident heat flux on helical coils at different tilt angles [26]. These conditions are expected to occur in parabolic dishes with coiled cavity receivers and will be investigated in the current study. Furthermore, inadequate literature was found concerning naturalistic experimental investigations of the performance of micro-scale direct steam generation using a solar dish. Micro-scale solar thermal Rankine cycles have not been investigated extensively since there is a gap in the steam turbine market at this scale (below 1 kW) due to their current inability to efficiently convert low mass flux steam to useful mechanical power. Recent developments of micro-scale steam expansion technology are promising and warrant further research into Rankine cycle solar collectors. The optical performance of a novel 2.7 m^2 stretched-membrane faceted concentrator used in the current work was previously investigated by Roosendaal et al. [27]. Using the novel concentrator, the potential for rural off-grid power generation and water pumping is investigated in the current work. This is achieved by carrying out a first and second law analysis of superheated steam generation at pressures above 3 bar in a helical cavity receiver connected to the concentrator.

(a)

(b)

Figure 1: Side view (a) and front view (b) of the experimental setup on the roof of Engineering Building 2 at the University of Pretoria. The modular solar dish concentrates the sun's rays onto the aperture of the insulated helically coiled solar cavity receiver for direct steam generation.

2. Experimental setup

An experimental setup was constructed to test the performance of a cavity receiver under realistic environmental conditions as shown in Figure 1. A flow diagram that describes the layout of the test facility is presented in Figure 2, where the main components and

measurement sensors of the test facility are numbered accordingly. The test facility comprises five sections: the pressure system, the solar tracker, the modular dish, the solar receiver and the measurement devices. The combination of the modular dish reflector and the solar receiver is referred to as the solar collector.

The pressure and flow rate of the steam through the process tubing was controlled by the pressure system. All the 304 stainless steel process tubing on the solar tracker (including the receiver coil) had an outer diameter of 13.26 mm and an inner diameter of 8.6 mm. Water was pressurised in a reservoir by feeding compressed air into the top of the reservoir at a regulated pressure. This allowed for a degree of control over the supply pressure from the receiver. The flow rate of the steam was then controlled by expanding it through a needle valve. The receiver's aperture was positioned at the calibrated focal point of the modular dish to maximise the intercept factor at the aperture.

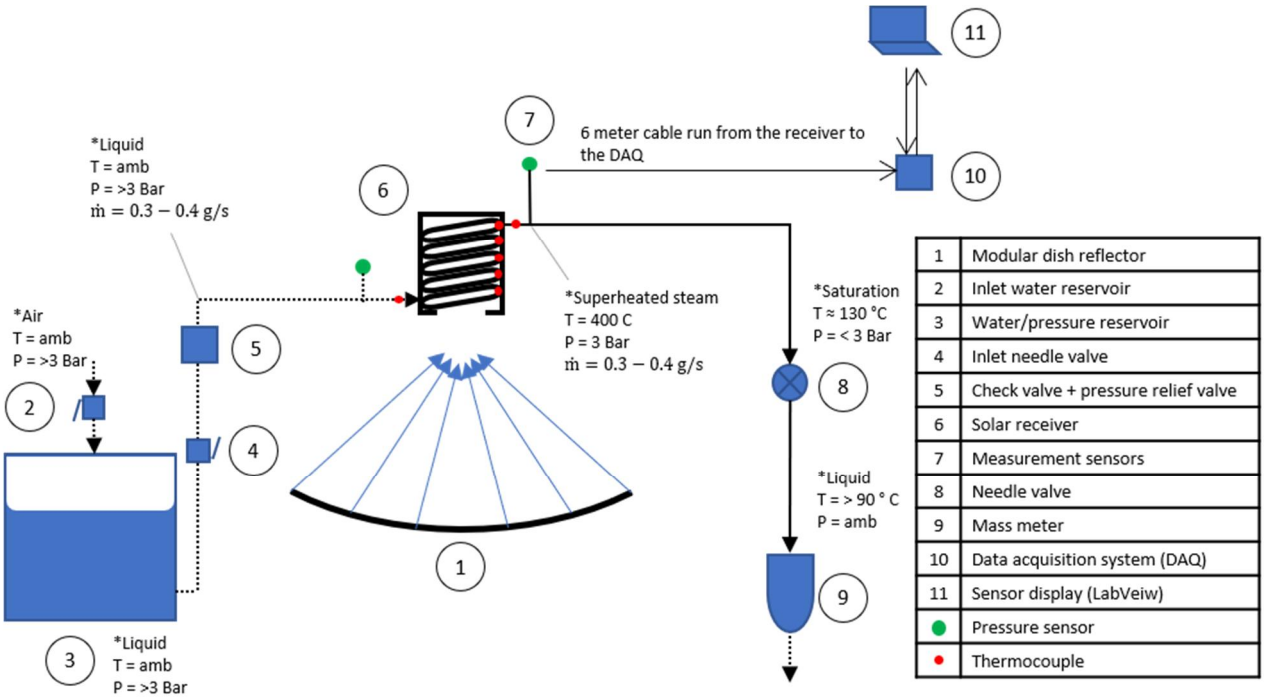

Figure 2: Schematic representation of the experimental test facility layout.

2.1 Solar receiver

The receiver coil had a uniform helical section at its base and a conical section at its top, as presented in Figure 3. The uniform helical section had an outer diameter of approximately 150 mm with a pitch of 13.26 mm and 12 coil turns along the helix. The coil was manufactured

from 304 stainless steel with an outer diameter of 13.26 mm and an inner diameter of 8.6 mm, to allow for local and low-cost manufacturing. The conical section was welded onto the uniform helix, and the outer diameter reduced from 150 mm to approximately 90 mm in four coil turns. The inlet and outlet process tubing extended from the outer diameter of the uniform helical section by 200 mm.

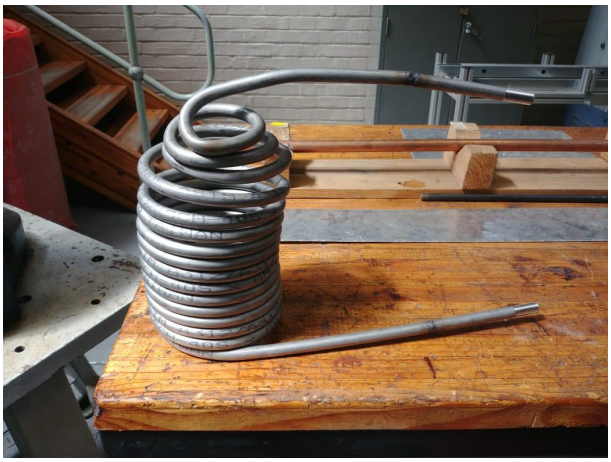

Figure 3: Constructed receiver coil.

To measure the fluid temperature within the receiver, eight WIKA TC 40 K-type thermocouple probes, with probe diameters of 3 mm each, were inserted at every second turn of the receiver coil, starting at the first turn located near the inlet. Two K-type thermocouple probes were also inserted at the inlet and outlet of the coil. The junctions of the thermocouples were positioned exactly at the centre of the coil tube to obtain precise measurements relative to the flow at the centre of the coil tube. The probes were held and sealed using 1/8-inch stainless steel compression couplings that were welded onto the outer surface of the tube. WIKA TC 40 K-type surface thermocouples were welded onto the inside and outside of the helical coil at the coil turns shown in Figure 4.

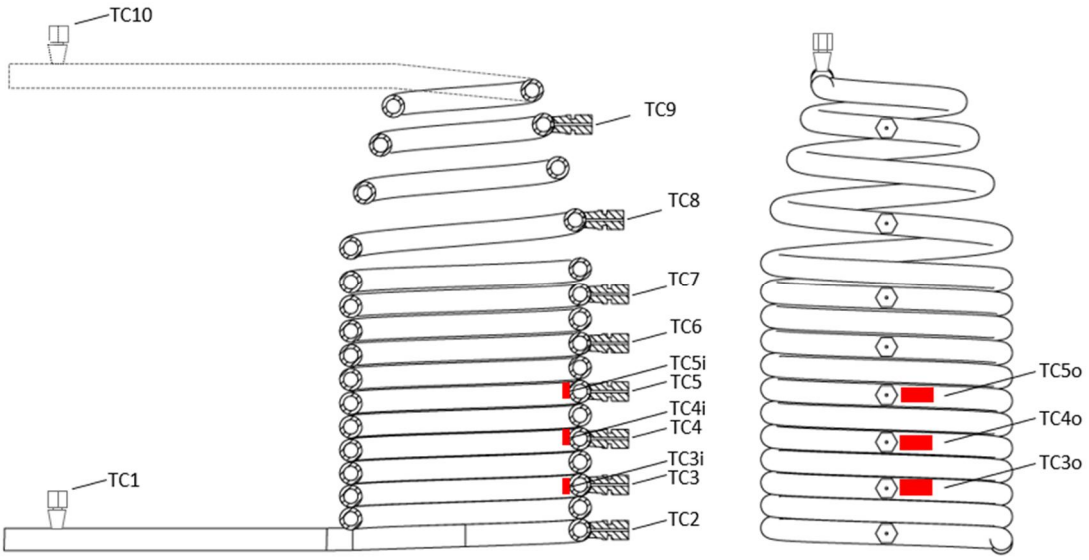

Figure 4: Thermocouple placement on the receiver coil.

A hydraulic pressure test was performed on the receiver coil and the process piping, where the piping was filled with water and taken to a pressure of 8 bar for two hours to check for leaks. Furthermore, a pneumatic pressure test was conducted on the receiver and process piping, where the pressure was increased to 4 bar for two hours.

The receiver cavity comprised a rectangular prism-shaped, mild steel supporting frame with 0.5 mm aluminium sheeting adhered and riveted to the supporting frame to create an airtight seal. The receiver cavity was mounted to the receiver arm through the mounting holes located near the aperture of the receiver. Den Braven fire sealant was used to adhere the aluminium sheet to the supporting frame. The cavity aperture and the cavity lid were not sealed with the aluminium sheeting. The lid of the cavity receiver allowed for the insertion of the cavity insulation and the receiver coil. The lid was a 3-mm-thick mild steel rectangular plate that could be screwed to the supporting frame using 5 mm butterfly screws.

The cavity insulation comprised 25-mm ceramic fibreboard and ceramic wool fibre, used as a filler. In total, 25 mm of ceramic fibre board covered the receiver coil, with an added 25 mm at the back and top of the cavity to serve as a channel for the thermocouple leads. The cavity aperture was circular and 135 mm in diameter with a 60° chamfer that served as a wind guard. An illustration of the receiver cavity is presented in Figure 5.

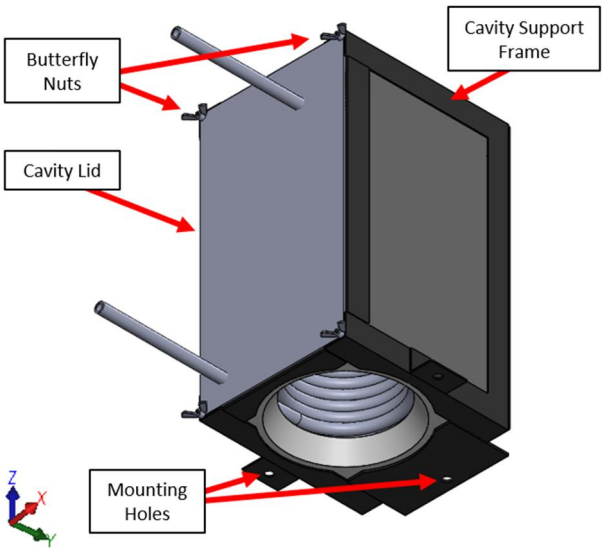

Figure 5: Illustration of the receiver cavity.

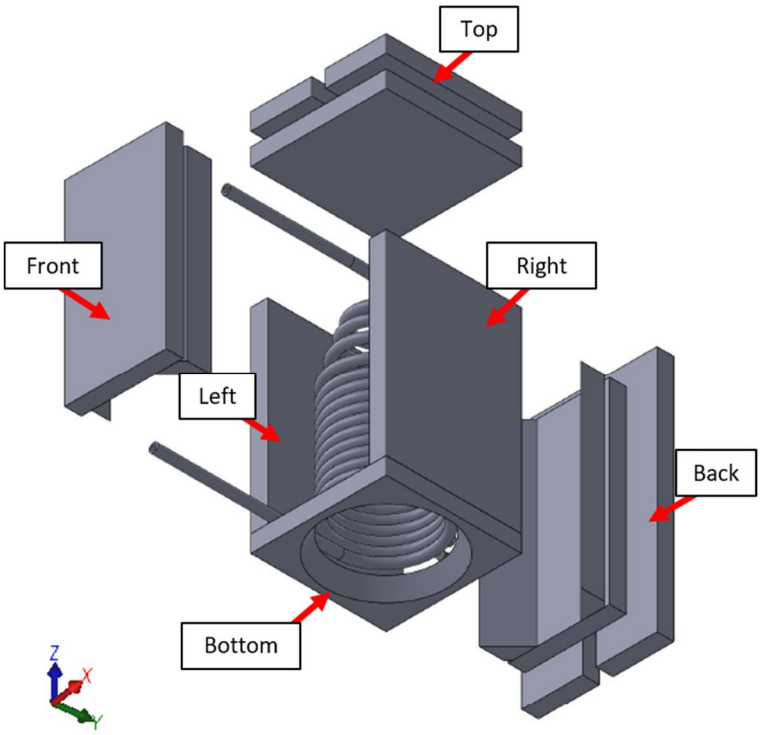

Figure 6: Exploded view of the receiver cavity depicting the sections of insulation.

The receiver cavity was constructed in such a way that two layers of 25-mm ceramic fibre insulation could be packed into the top and back sections, and a single layer could be packed into the remaining sections, as depicted in Figure 6.

2.2 Pressure system

A 12-bar compressed air line was used as the pressure supply for the experiments. An air regulator was connected between the air supply line and the water reservoir, using a pneumatic hose as presented in Figure 7. This was done to have tight control over the supply pressure of the superheated steam coming out of the receiver during experimentation. Two 10-bar Honeywell PX2-series pressure transmitters were placed in line at the inlet and outlet of the receiver coil to determine the pressure states of the water or steam at the inlet of the receiver and the superheated steam at the outlet.

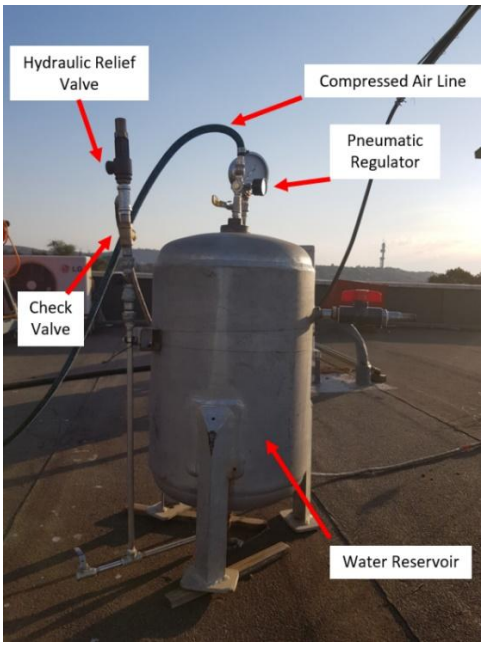

Figure 7: Water reservoir used during experimental testing.

The temperature of the superheated steam coming out of the receiver was far beyond the temperature limit of the pressure transmitter. Special attention was therefore paid to extend the pressure transmitter away from the primary flow. This was done using a U-shaped thermal syphon that would capture the steam condensate and provide a static barrier between the outlet pressure transmitter and the process steam. This static barrier would function as a heat sink, whereby the heat being conducted from the process flow through the static condensate would be transferred to the environment through convection. An illustration of the U-shaped thermal syphon is presented in Figure 8. The process inlet and outlet pipes extend outwards from the figure.

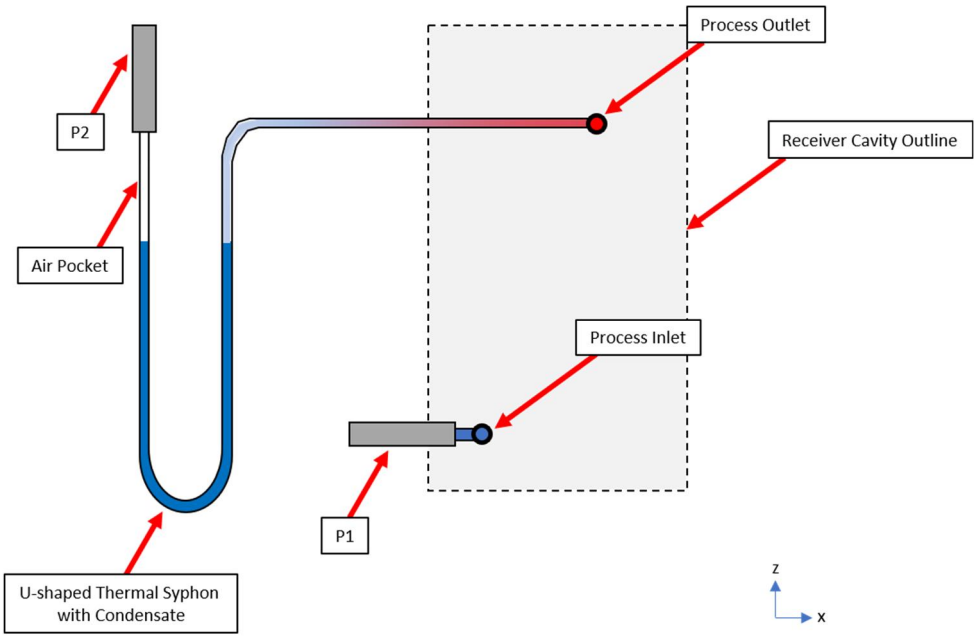

Figure 8: Schematic of the U-shaped thermal syphon and the inlet and outlet pressure transmitters.

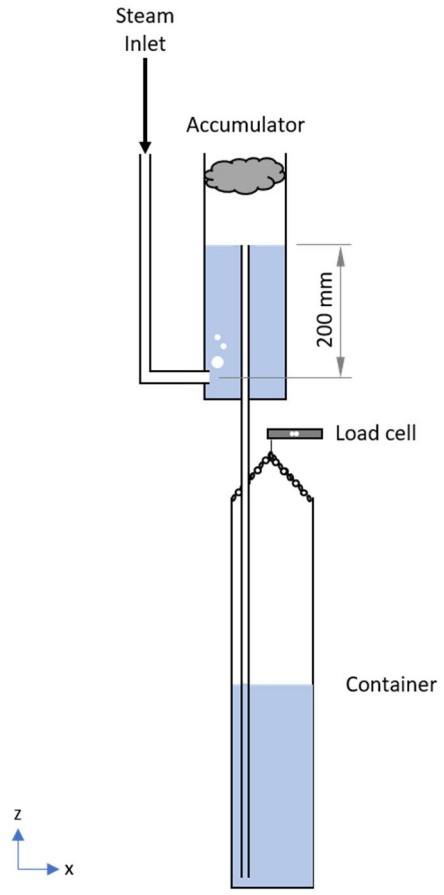

Figure 9: Schematic of the liquid mass meter.

The steam was then expanded through a needle valve and passed into a hydraulic accumulator just above atmospheric pressure, as presented in Figure 9. The accumulator was a steel container with an inlet at the bottom and an overflow pipe with an aperture 200 mm above the inlet. As the steam bubbled through the water in the accumulator, it condensed into a liquid, and the water level inside the accumulator rose until it flowed into the overflow pipe. As an added measure, a stainless-steel mesh, placed above the accumulator, would capture any escaping steam and transfer it back into the contained water. The overflow pipe channelled the overflow into a mass meter container. The mass meter was a secondary container that was attached to a 20 kg HX711 load cell. This ensured that shock from the collapsing steam bubbles was mitigated from the load cell readings, and the liquid mass accumulation over the testing period could be determined accurately.

2.3 Solar tracker

The experimental analysis made use of a two-axis solar tracker that had been constructed on the roof of the University of Pretoria's Engineering 2 Building. The solar tracker's elevation angle was adjusted using a linear actuator connected to the tracker's arm, and the azimuth angle was adjusted using a rotary actuator fixed to the tracker's base. The tracking of the sun was performed manually during testing. A simple visual tracking technique was used, whereby a directional pinhole, attached to the tracker, let a finite amount of sunlight through it. This light was projected onto a flat, semi-transparent target surface with a calibrated centre point as shown in Figure 10. The pinhole light was kept within a certain radius from the centre point on the target surface to maintain a tracking accuracy below 1°.

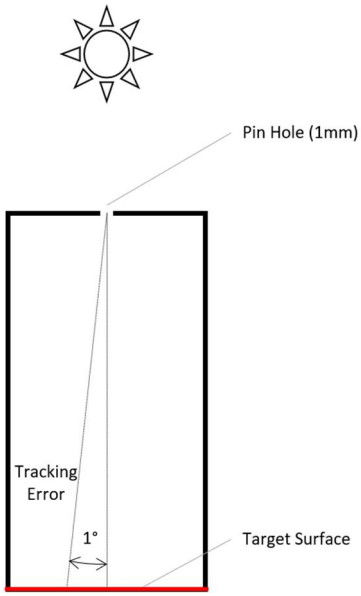

Figure 10: Schematic of the pinhole tracker used to track the sun within 1° of accuracy.

Since the length of the tracking device was 300 mm, the projected pinhole light would have to be kept within a 5.24 mm radius on the target surface for the tracker to have an accuracy below 1°. The tracking error is calculated using Equation (1).

$$TrackError = \tan^{-1}(5.24/300) \approx 1° \quad (1)$$

2.4 Modular solar dish

The modular dish comprises six smaller vacuum-membrane dish facets that work independently to concentrate the sun's direct normal irradiance (DNI) towards a calibrated focal point as described by Roosendaal et al. [27]. Each facet comprised a 50 μm Mylar sheet membrane, stretched and sealed over the elliptical rim of an off-the-shelf television satellite dish, forming a narrow cavity in which a vacuum could be drawn to pull the Mylar sheet membrane into a concave shape. A pneumatic valve, comprising a 1/4 inch threaded nipple, a quarter-turn valve and an 8-mm hose nipple, was inserted into the back of the dish, through which a vacuum could be drawn. All the connections at the back of the dish, including the dish mount and the pneumatic valve, were sealed with general-purpose silicone to prevent leaks.

The work of Zanganeh et al. [28] suggests that elliptical facets are beneficial since the tilting of the reflector facet to face the receiver aperture results in the projection of a near-circular image onto the receiver aperture plane because of the angularity between the incident solar

rays and the tilted reflector facet. This more closely resembles an image projected by an ideal parabolic dish. The total incident area of the elliptical facets was A_{dish} = 2.70 m^2 [27]. The advantages of the design are the low building costs and modularity, which allow for different dish shapes to be considered in a single experimental analysis. This is achieved by simply adjusting the reflector facets both in position and in facet concavity through the vacuum that is formed.

The six reflector facets were mounted onto arms that were subsequently connected to the central hub of the solar tracker. Each arm was tilted roughly 15° towards the central axis of the modular reflector. The facets were then tilted a further 7.5° towards the central axis of the modular reflector, resulting in a total tilt angle of 22.5° for each facet. This was done to obtain an effective rim angle of 45° [29-32].
The centroids of the reflector facets were positioned 800 mm from the central axis, which allowed the reflector to have an effective diameter of 1.6 m and a total diameter of 2.36 m, as presented in Figure 11. Because of the 45° effective rim angle, the focal point is positioned 800 mm above the horizontal plane of the centroids for the dish facets. The intercept factor (*IF*) of the setup was determined using a lunar testing method as described by Roosendaal et al. [27].

The spectral reflectivity of the Mylar sample was calculated to be 97% according to Roosendaal et al. [27], using ultraviolet and visible light (UV/VIS) spectrometry analysis using a CARY 100 Bio [33]. It is important to note that the spectrometry analysis was performed on a clean Mylar sample that had not been weathered. The study of Stine and Harrigan [31] showed that the reflectivity of the reflector material decreases with time due to exposure to weather.

2.5 Weather and solar irradiance measurement

The irradiance and ambient temperature measurements were taken using a SOLYS 2 sun tracker, positioned on top of the University of Pretoria's Engineering Building 1 as part of the South African Universities Radiometric Network (SAURAN) [34]. The SOLYS tracker was estimated to have a measurement accuracy of 2% [35]. The wind direction and velocity at the experimental facility were measured using the Ambient Weather WS-100X-WiFi weather station, located adjacent to the solar collector.

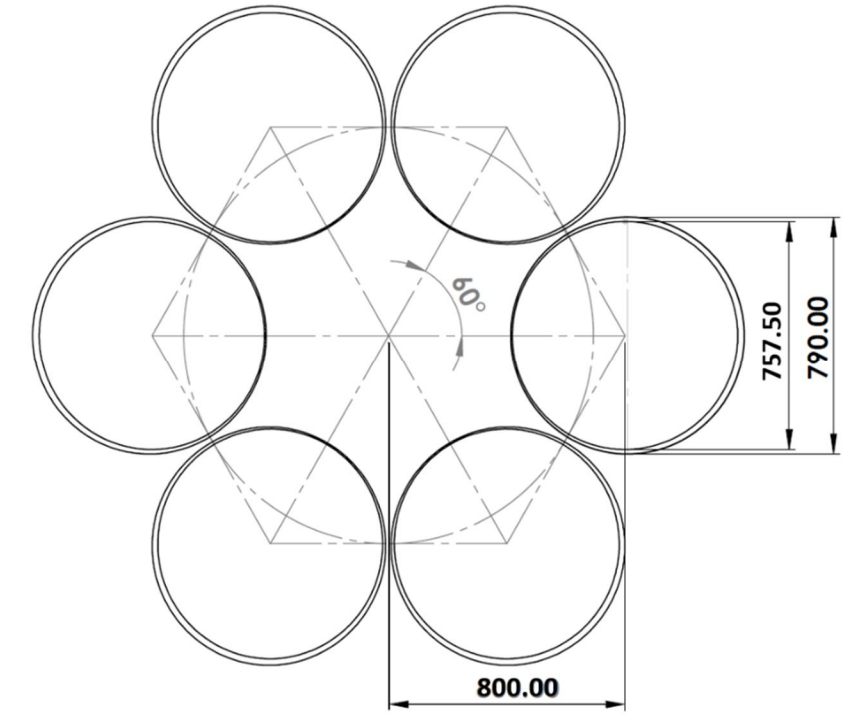

(a)

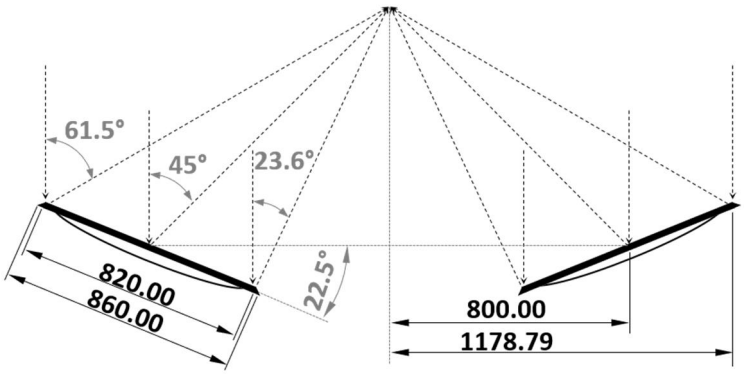

(b)

Figure 11: Dish layout and dimensions with (a) a top view; and (b) a sectioned front view with facet rim angles, respectively.

2.6 Experimental method

The cavity receiver was tested on a clear, sunny day. The solar collector was orientated towards the sun so that all the reflected images from the dish reflector's facets could intercept the aperture. The pinhole tracker was then fixed in place on the solar tracker with the light from the pinhole projected onto the cross-hairs of the target. As the sun moved

across the sky, light from the pinhole tracker showed the degree of misalignment between the solar collector and the sun. The solar collector was adjusted manually to keep the pinhole tracker within the 1° tracking boundary. This resulted in the collector having a tracking error of less than 1° during testing.

The water contained within the pressure reservoir was pressurised using regulated, compressed air, which allowed for a degree of control over the supply pressure at the inlet of the receiver coil. The water was then heated using concentrated radiation from the modular dish and turned into steam. In proceeding coil turns, the steam was superheated and passed through the outlet of the receiver.

With the receiver aperture positioned at the focal point of the modular dish, a near steady-state period was observed during testing, where the inlet and outlet temperature readings became constant. The K-type thermocouples that were placed throughout the coil length measured the temperature of the steam. Pressure sensors positioned at the inlet and outlet of the receiver coil measured the steam pressure. Note that sensor calibration is discussed in Appendix A. Using the temperature and pressure measurements, the energetic and exergetic states of the steam could be determined. The surface K-type thermocouples that were welded onto the inside and outside of the coil measured the wall temperature gradient of the coil tube. Once a steady-state irradiance period was determined, the supply pressure was increased, and the flow rate decreased until steady-state superheated steam was produced in the receiver. A target supply pressure of 3 bar was used in the experiments with a target flow rate of 0.32 g/s.

3. Mathematical model

An analytical model is presented that will be used to characterise the performance of the solar collector. The analysis model was used to determine the first- and second-law efficiency of the receiver. A heat-loss model is presented to define the components of heat loss in the receiver.

3.1 First-law efficiency

The heat transfer rate that is present at the receiver tube must account for losses from the receiver in which there are conduction, convection and radiation heat losses. This is expressed in the energy balance given in Equation (2).

$$\dot{Q}_{net} = \dot{Q}_{ap} - \dot{Q}_{cond,loss} - \dot{Q}_{conv,loss} - \dot{Q}_{rad,loss} \quad (2)$$

If the components of heat loss are not estimated, the loss terms may be replaced by a single loss term, as expressed in Equation (3).

$$\dot{Q}_{net} = \dot{Q}_{ap} - \dot{Q}_{loss} \quad (3)$$

The net heat transfer rate captured by the working fluid in the coiled tubes is expressed in Equation (4).

$$\dot{Q}_{net} = \Delta H_w = \dot{m}_w(h_{w,out} - h_{w,in}) \quad (4)$$

Considering the incident solar radiation on the dish reflector and the intercept factor of the collector and the reflectivity of the reflector facets (η_{ref}), the total radiation intercepted at the aperture of the receiver can be expressed using Equation (5).

$$\dot{Q}_{ap} = IF \times \eta_{ref} I_{sun} A_{dish} \quad (5)$$

The fundamental energy conservation equation is expressed using Equation (6). It describes how the net energy absorbed by the receiver changes the energy state of the working fluid that flows through the coils.

$$\dot{Q}_{net} = IF \times \eta_{ref} I_{sun} A_{dish} - \dot{Q}_{loss} = \dot{m}_w(h_{w,out} - h_{w,in}) \quad (6)$$

The thermal efficiency of the receiver is expressed as a fraction of the net heat transfer rate into the working fluid over the intercepted radiation that is reflected from the dish and expressed in Equation (7).

$$\eta_{th,rec} = \frac{\dot{Q}_{net}}{\dot{Q}_{ap}} = \frac{\dot{m}_w(h_{w,out} - h_{w,in})}{IF \times \eta_{ref} I_{sun} A_d} \quad (7)$$

The thermal efficiency of the collector is determined by considering Equation (8).

$$\eta_{th,col} = \frac{\dot{Q}_{net}}{\dot{Q}_{sun}} = \frac{\dot{m}_w(h_{w,out} - h_{w,in})}{I_{sun}A_d} \quad (8)$$

3.2 Second-law efficiency

The expression for the exergy state of the working fluid is given in Equation (9) where the change in exergy of the working fluid is expressed using Equation (10).

$$\Psi_w = \dot{m}_w[(h_w - h_\infty) - T_\infty(s_w - s_\infty)] \quad (9)$$

$$\Delta\Psi_{\mathrm{w}} = \Psi_{\mathrm{w,out}} - \Psi_{\mathrm{w,in}} \quad (10)$$

The general expression of available work due to the heat transfer rate is defined using Equation (11).

$$\Phi = \dot{Q}\left[1 - \frac{T_\infty}{T_s}\right] \quad (11)$$

According to Onyegegbu and Morhenne [36], the available work due to solar radiation is given in Equation (12).

$$\Phi_{sun} = \dot{Q}_{sun}\left[1 - \frac{4T_\infty}{3T_{sun}}\right] \quad (12)$$

The temperature T_{sun} is the black body temperature of the sun, which may be approximated to be between 6 000 and 5 762 Kelvin [37]. The second-law efficiency may then be determined using Equation (13), which provides an effective means of determining the performance of the receiver.

$$\eta_{2nd} = \frac{\Delta\Psi_{\mathrm{w}}}{\Phi_{sun}} \quad (13)$$

The associated irreversibility is defined as the negative of the summation of the changes in exergy as presented in Equation (14).

$$\bar{I} = -1 \times (\Delta\Psi + \Delta\Phi + \Delta\mathrm{W}) \quad (14)$$

3.3 Heat loss model

The fundamental components of heat loss in a cavity receiver are convection heat loss through the cavity aperture, radiation heat loss through the cavity aperture and conduction heat loss through the cavity insulation. These heat loss components are illustrated in Figure

12, which shows the heat loss mechanisms, as well as the intercepted radiation, through a receiver aperture.

3.3.1 *Convection heat loss model*

The convection heat loss model is divided into two components: the natural convection heat loss ($\dot{Q}_{loss,natural}$) and the forced convection heat loss ($\dot{Q}_{loss,forced}$). Natural convection heat loss occurs due to buoyancy forces from the air being heated within the cavity receiver and escaping through the aperture.

The forced convection component occurs due to the effect of wind blowing over the receiver aperture, resulting in convection heat loss. Assuming that the two components are independent of one another, they are summated, resulting in total convection heat loss from the aperture of the receiver, as shown in Equation (15) [38].

$$\dot{Q}_{conv,loss} = \dot{Q}_{loss,natural} + \dot{Q}_{loss,forced} \tag{15}$$

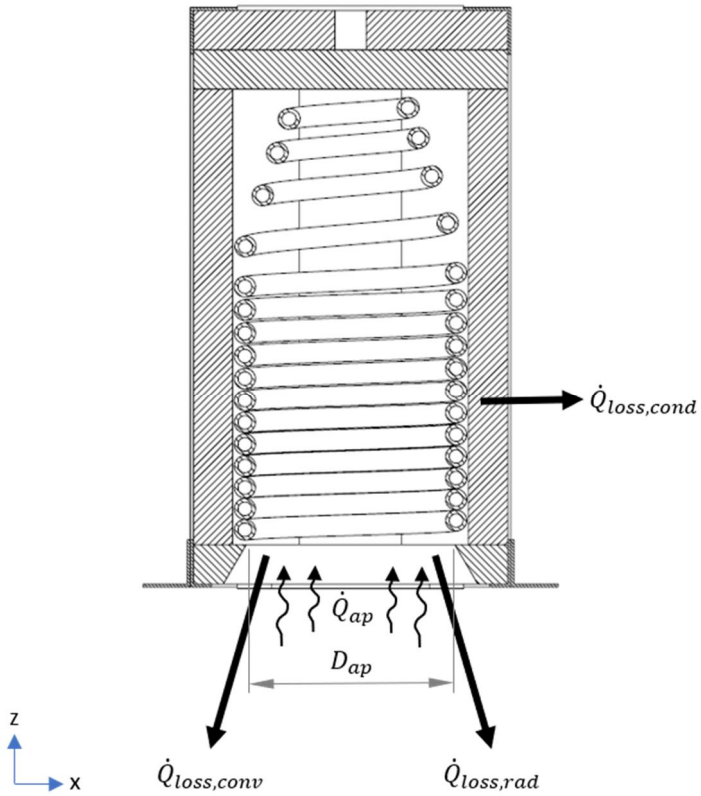

Figure 12: Schematic of heat losses present in a cavity receiver.

The correlation of Stine and McDonald [32], presented in Equation (16), was used to determine the Nusselt number for the natural convection heat loss from the receiver aperture. It should be noted that $L_c = D_{cav,i}$ and that $T_{prop} = T_\infty$. The cavity tilt angle (θ) is the angle between the normal surface from the aperture and the horizontal plane.

$$Nu_{natural} = 0.088 Gr^{1/3} \left(\frac{T_s}{T_\infty}\right)^{0.18} \cos^{2.47}(\theta) \left(\frac{D_{ap}}{L_c}\right)^{1.12-0.98\left(\frac{D_{ap}}{L_c}\right)} \quad (16)$$

Many numerical studies show that side-on wind, parallel to the receiver aperture, results in the greatest heat loss regardless of the receiver tilt angle [39-41]. Studies show that wind effects on the forced convection heat loss can increase to three to four times that of natural convection if a wind-skirt is not used [38, 42].

If a wind skirt is used, the forced convection heat loss is estimated to be twice that of natural convection heat loss at wind speeds below 4.5 m/s [42]. Ma [38] further suggested that the natural and forced convection heat losses can simply be added together, as presented in Equation (17), for the condition of side-on wind flow since the vectors of natural and forced convection are relatively perpendicular to one another.

$$\bar{h}_{conv} = \bar{h}_{forced} + \bar{h}_{natural} \quad (17)$$

The convection heat loss from the aperture may be calculated using Equation (18). The i-subscript denotes the forced and natural convection components.

$$\dot{Q}_{loss,i} = \bar{h}_i A (T_s - T_\infty) \quad (18)$$

The area (A) was defined to be the total exposed surface area inside the receiver cavity. This includes the exposed cavity walls in the receiver [38]. The forced convection heat loss component was determined using the area considered in the natural convection heat loss.

3.3.2 *Radiation heat loss model*

The radiation heat loss ($\dot{Q}_{rad,loss}$) was estimated by considering the reflected radiation from the receiver cavity, as well as the emitted radiation for the receiver coils, as presented in Equation (19). The reflected radiation component is a function of the optical properties of the receiver coil, as well as the receiver geometry. It was assumed that the inner cavity reflected the incident radiation in a diffuse manner. The total reflected radiation heat loss was thus

determined using Equation (20). The emitted radiation heat loss from the aperture was determined using Equation (21). The temperature of the surroundings was approximated to be equivalent to the ambient temperature. The average emissivity and absorptivity of the receiver cavity were estimated to be equivalent to that of the stainless steel coil in the receiver.

$$\dot{Q}_{rad,loss} = \dot{Q}_{ref,loss} + \dot{Q}_{emit,s-ap} \tag{19}$$

$$\dot{Q}_{ref,loss} = \rho_{steel} F_{s-ap} \times \dot{Q}_{ap} = \rho_{steel} F_{s-ap} \times IF \eta_{ref} I_{sun} A_{dish} \tag{20}$$

$$\dot{Q}_{emit,s-ap} = \frac{\sigma(T_s^4 - T_{ap}^4)}{\left[\frac{1-\varepsilon_s}{A_s \varepsilon_s} + \frac{1}{A_s F_{s-ap}} + \frac{1-\varepsilon_{ap}}{A_{ap}\varepsilon_{ap}}\right]} \tag{21}$$

The aperture was considered to be a two-dimensional surface with a surface temperature equal to the average surface temperature of its surroundings and had an approximated emissivity of 1. The view factor between the inner cavity and the aperture was determined by approximating the inner cavity as a cylinder with a conical top. A schematic of the simplified inner cavity is presented in Figure 13. The inner cavity diameter was adjusted to be the inner coil diameter rather than the diameter of the insulation walls. The view factor between the inner cavity and the aperture was determined to be $F_{s-ap} \approx F_{2,4-1} = 0.17$.

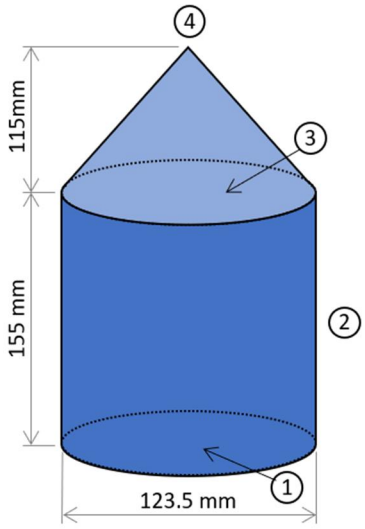

Figure 13: Simplified inner cavity surface for determining view factors.

3.3.3 *Conduction heat loss model*

The total conduction heat loss was broken up into heat loss components for each wall of the cavity (see Figure 6) according to Equation (22).

$$\dot{Q}_{cond,loss} = \dot{Q}_{loss,front} + \dot{Q}_{loss,back} + \dot{Q}_{loss,top} + \dot{Q}_{loss,bottom} + \dot{Q}_{loss,left} + \dot{Q}_{loss,right} \quad (22)$$

The conduction heat loss through the cavity insulation was modelled by considering the conduction mechanism through the insulation medium, as well as the convection mechanism present on the outside of the receiver cavity. This is evident in the thermal resistance (R_{tot}) presented in Equation (23).

$$\dot{Q}_{cond,loss} = \frac{T_s - T_\infty}{R_{total}} = \frac{T_s - T_\infty}{\frac{t_{ins}}{k_{ins}A_{ins,in}} + \frac{1}{\bar{h}A_{ins,out}}} \quad (23)$$

The convection heat transfer coefficients on the outer surfaces of the receiver cavity were determined using the correlation for convection over a flat plate. The convection heat transfer coefficient is dependent on the orientation of the dish with respect to the wind. For that reason, the following correlations were considered:

For forced convection over surfaces that are parallel to the wind velocity, the correlations for laminar and turbulent flow over a flat plate, given in Cengel and Ghajar [43], were used and are presented in Equations (24) and (25) respectively.

$$Nu = \frac{\bar{h}L}{k} = 0.664 Re_L^{0.5} Pr^{1/3} \quad (24)$$

$$Nu = \frac{\bar{h}L}{k} = 0.037 Re_L^{0.8} Pr^{1/3} \quad (25)$$

For forced convection on the front, back and sidewalls, the Nusselt number is estimated using the correlation for cross-flow on a square tube perpendicular to the wind velocity in Equation (26) and the correlation for cross-flow on a square tube tilted 45° to the wind velocity in Equation (27) [44].

$$Nu = \frac{\bar{h}L}{k} = 0.094 Re_L^{0.675} Pr^{1/3} \tag{26}$$

$$Nu = \frac{\bar{h}L}{k} = 0.258 Re_L^{0.635} Pr^{1/3} \tag{27}$$

For natural convection from the outer surfaces of the receiver cavity, the tilt angle must be considered. The correlation, given in Cengel and Ghajar [43], is thus considered and presented in Equation (28). This expression describes the natural convection heat transfer rate for inclined plates with a laminar boundary layer that forms over the plate's surface.

This phenomenon typically occurs on the bottom surface of an inclined heated plate and is comparable to the natural convection heat transfer rate that occurs for vertical plates.

$$Nu = \frac{\bar{h}L}{k} = 0.59 {Ra_L}^{1/4} \cos^{1/4}(\varphi) \tag{28}$$

The inclination angle (φ), also known as the azimuth angle, is considered to be the angle between the vertical axis and the normal surface. The natural convection that occurs at the top surface of an inclined heated plate was investigated by Fujii and Imura [45], and the correlation – considering a 300 mm plate – was determined. This is presented in Equation (29).

$$Nu = \frac{\bar{h}L}{k} = 0.13\left[(Gr_L Pr)^{1/3} - (Gr_c Pr)^{1/3}\right] + 0.56(Gr_c\, Pr\, cos\varphi)^{1/4} \tag{29}$$

The characteristic Rayleigh number ($Gr_c Pr$) was used in the correlation to represent the transition regions along the plate where buoyancy forces caused boundary layer separation, resulting in the Nusselt number diverging from the characteristic of the laminar region. The transitional region was determined in the work of Vliet [46]. The characteristic Rayleigh number was determined by calculating an average value between the upper and lower intervals presented by Vliet [46] for the given angle of inclination.

When considering the combined natural and forced convection components, the correlation, given in Cengel and Ghajar [43], is used and presented in Equation (30). The exponent n tends to be roughly 3 for vertical surfaces and 4 for horizontal surfaces in experimental data.

$$Nu_{combined} = \frac{\bar{h}L}{k} = \left(Nu_{forced}^{n} \pm Nu_{natural}^{n}\right)^{1/n} \quad (30)$$

The characteristic length differs, depending on the correlation used for natural and forced convection. For this reason, the characteristic length of the combined Nusselt number was determined by considering the weighted average of the characteristic lengths used during the natural and forced convection Nusselt number calculations, as presented in Equation (31).

$$L_{c,combined,i} = \left[L_{c,forced,i} \times \frac{Nu_{forced,i}^{n}}{Nu_{forced,i}^{n} + Nu_{natural,i}^{n}} + L_{c,natural,i} \times \frac{Nu_{natural}^{n}}{Nu_{forced,i}^{n} + Nu_{natural,i}^{n}}\right] \quad (31)$$

$$T_{ins,out} = T_{ins,in} - \dot{Q}_{cond,loss} \times \frac{t_{ins}}{k_{ins}A_{ins,in}} \quad (32)$$

The conduction heat loss was determined through an iterative process presented in Figure 14. The process was repeated until an iteration change of 0.001 °C was noted for the surface temperature of the outer cavity. The inner cavity temperature ($T_{ins,in}$) was approximated to be equivalent to the average coil surface temperature. An initial estimate of the outer cavity temperature ($T_{ins,out}$) was made, being the average temperature between the inner cavity temperature and the ambient temperature. Due to the solar collector being orientated roughly at 45° to the wind direction for most of the testing period, Equation (32) was used to describe the forced convection heat loss from the cavity sides. Furthermore, the thermal conductivity of the ceramic fibre board insulation was provided by the manufacturers as a function of temperature [47].

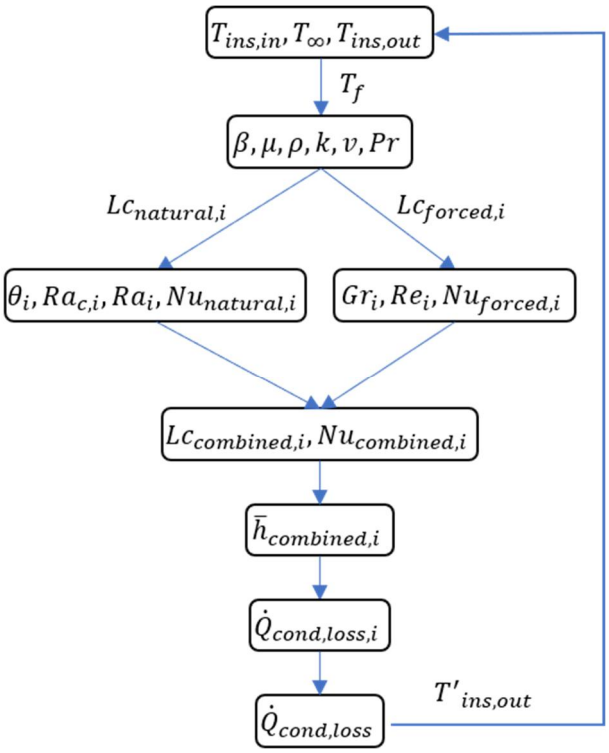

Figure 14: Conduction heat loss solution methodology.

4. Experimental results

On the testing date of 20 September 2019, the weather was sunny and clear, with low wind velocities. A near steady-state period of 91 minutes was obtained, between 13:19 and 14:50, when the DNI, the receiver inlet and exit temperature, and the steam mass flow rate were maintained at constant values within a specific tolerance. The wind was measured to flow at speeds of between 0 and 3.9 m/s, with the direction oscillating in a full 360° range.

An observation was made during testing where only the first seven coil turns experienced incident radiation directly from the dish reflector. This is evident in Figure 15. From this observation, it is expected that thermocouple TC 5, which is positioned on the seventh coil turn, should have the highest average temperature of the 16 coil turns if the cavity temperature is lower than TC 5. This is because a net heat loss would begin to occur after the seventh coil turn due to the temperature difference between the subsequent coil turns and the surroundings.

Figure 15: Incident solar radiation on the receiver coils during testing.

4.1 Solar irradiance

The DNI had a slight negative gradient during the testing period, as shown in Figure 16. However, this was taken to be an acceptable decrement, since the irradiance only reduced by 12.5% over the entire period. An average reading of 757.13 W/m^2 was observed for the testing period.

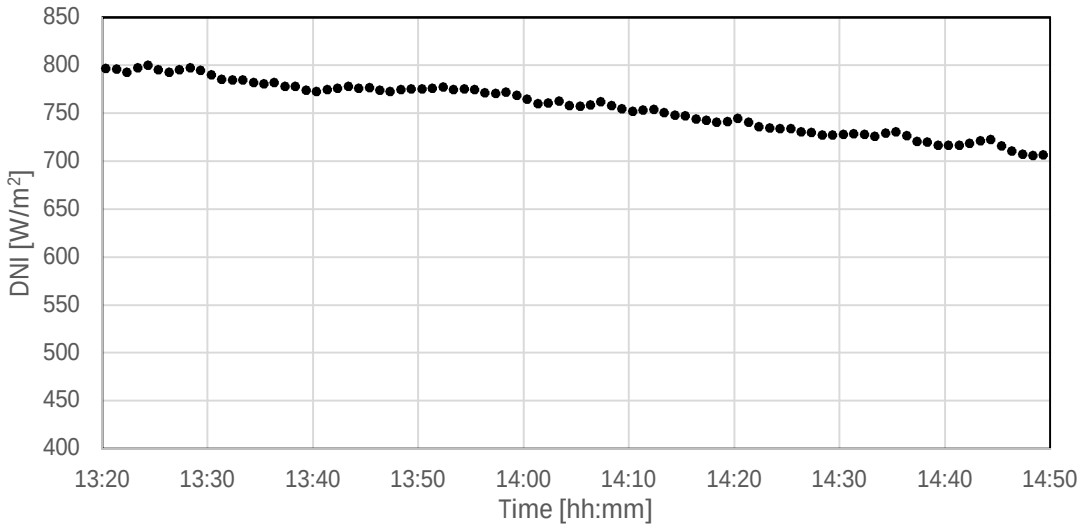

Figure 16: Direct normal irradiance measurements over the testing period.

4.2 Mass flow rate

Figure 17 indicates that the mass accumulation of the condensate at the outlet over the 91 minutes followed a constant linear trend, with a gradient of 0.2938 g/s. The gradient of the linear trend represents the constant mass flow rate, with a 98% linear correlation.

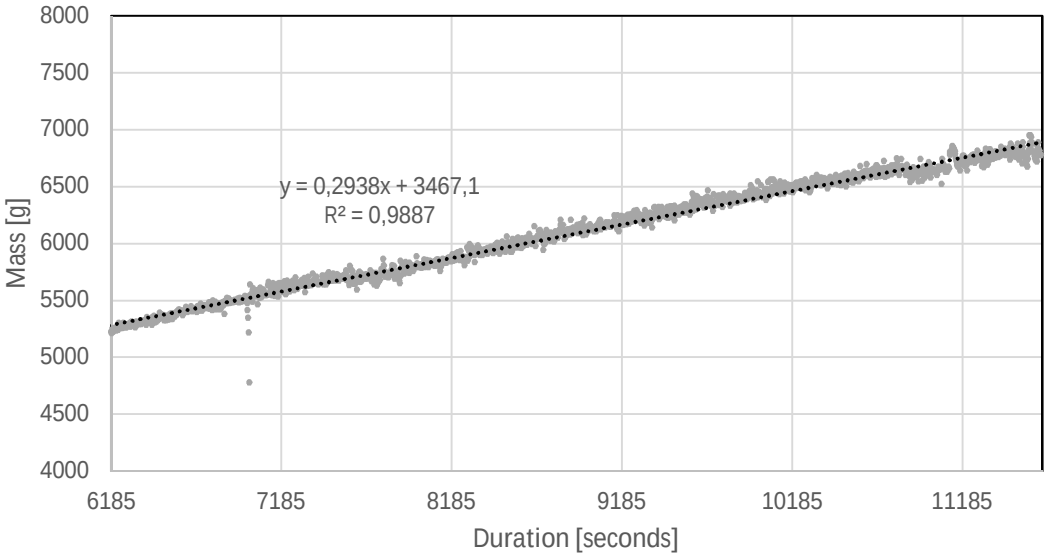

Figure 17: Mass accumulation at the outlet of the solar collector during the testing period.

4.3 Pressure

A steady-state pressure condition could not be achieved during testing, as is evident in the plotted measurements in Figure 18. The pressure appeared to pulsate between the supply pressure at the minimum and a maximum of roughly 2.5 bar above the supply pressure. The period of pulsation ranged between 1.5 and 2 minutes. The supply pressure was set to 3 bar at the beginning of testing and then readjusted to 3.2 bar at 13:54, since a notable decrement was observed.

Another observation that can be made from these results is that the inlet pressure (P1) is slightly lower than the outlet pressure (P2). This is counter-intuitive, since a higher supply pressure is required to move the liquid through the coil towards the outlet, and the pressure transmitters were placed directly next to the inlet and outlet of the receiver. The pressure drop through the coil is expected to be negligible due to the low mass flow rate and therefore the observation can be attributed to the handling error (see Appendix A). The average

pressure between P1 and P2 oscillated between a maximum of 595 and 280 kPa during the testing period.

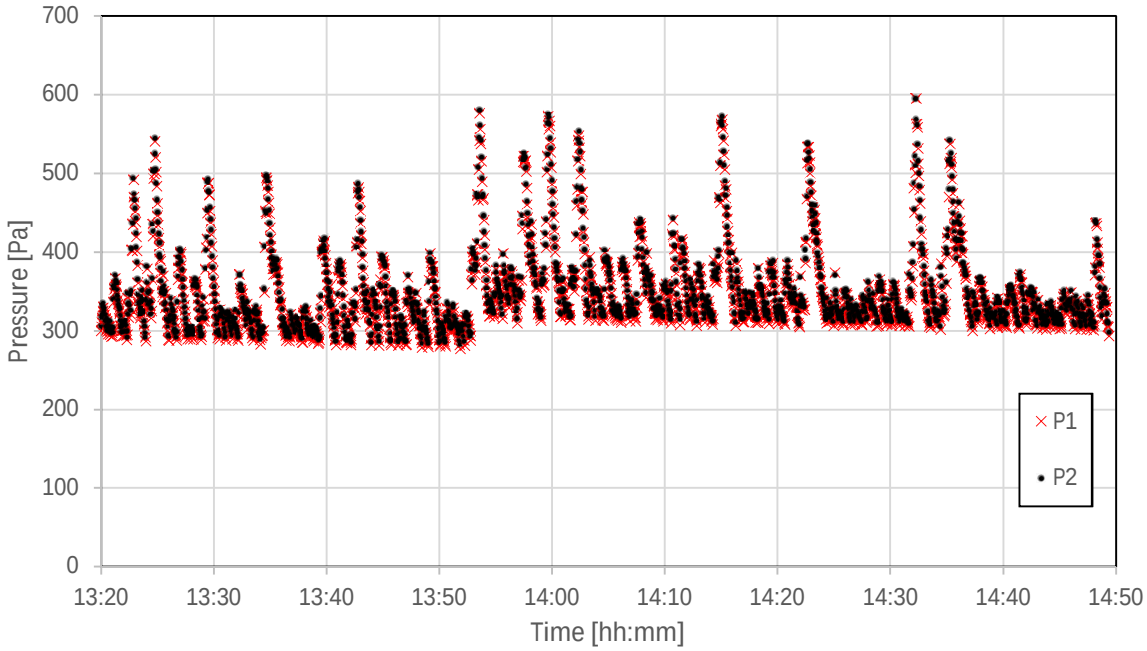

Figure 18: Pressure measurements taken over the testing period.

4.4 Temperature

Steam temperature measurements were taken using the insertion thermal couples positioned at every odd coil turn. The measurements of TC 1 to TC 10 are plotted in Figure 19. A summary of the results is presented in Table 1. A steady inlet temperature of 54 °C is observed at TC 1. As the water flows through the subsequent coil turns that are exposed to the concentrated solar radiation, the respective thermocouples measure an erratic oscillation in temperature. It may be observed that TC 3 primarily exists in the saturation region with an average temperature of 139 °C, after which the erratic oscillations continue until the temperatures stabilise after TC 7 to an average value of 355.2 °C among TC 7, TC 8 and TC 9. Another interesting observation is that the average steam temperature after TC 6 decreases within the receiver until it reaches the outlet at TC 10, where the steam temperature rapidly decreases to an average temperature of 163.1 °C. The average coil surface temperature within the cavity was determined to be 315.8 °C by summating the time-averaged coil temperatures for TC 2 to TC 9 over their respective coil lengths.

The time-averaged temperatures of the steam are plotted along the coil length in Figure 20. Error bars show the 95th and 5th percentile of the measurement distribution around the given temperature averages. The plot shows the temperature oscillations that occur at TC 2, TC 4 and TC 5 and the sudden drop in temperature after TC 9.

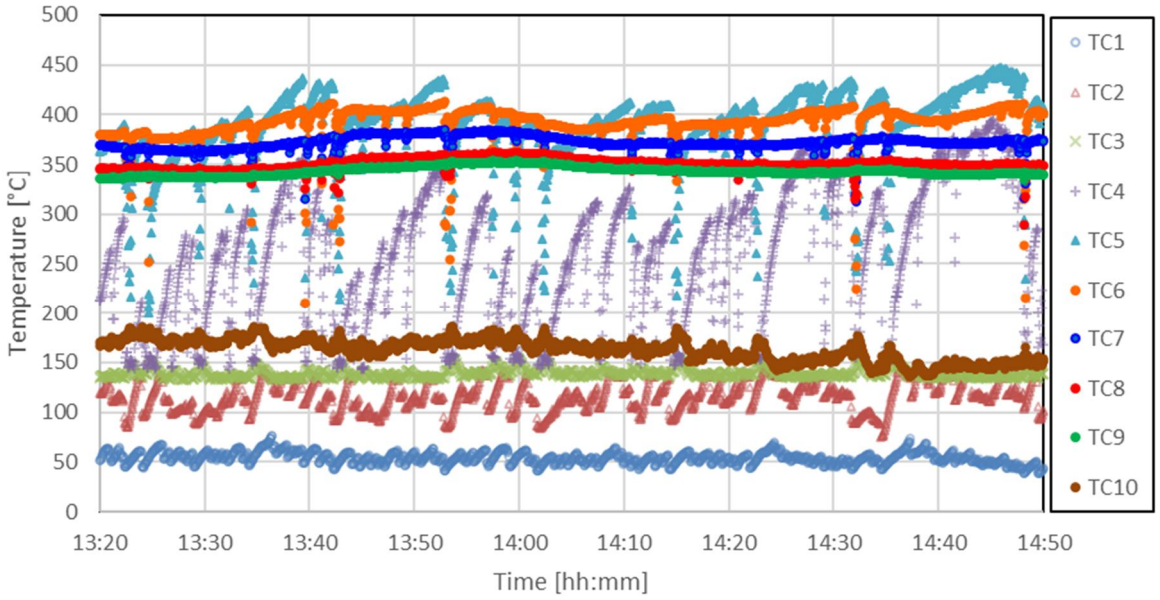

Figure 19: Insertion thermocouple measurements over the testing period.

Table 1: Summary of insertion thermocouple measurements over the testing period

Thermocouple	Average (°C)	Maximum (°C)	Minimum (°C)	Standard deviation (°C)
TC 1	54.1	76.2	38.8	5.8
TC 2	117.0	147.6	75.0	15.0
TC 3	139.0	154.4	132.2	4.4
TC 4	258.1	395.7	139.7	68.7
TC 5	389.1	446.8	199.6	38.6
TC 6	391.5	413.5	211.0	17.6
TC 7	371.8	384.9	312.1	7.0
TC 8	350.6	362.0	289.6	5.5
TC 9	343.1	353.6	335.1	4.5
TC 10	163.1	186.5	135.9	10.9

Figure 21 presents the thermocouple readings of TC 4 and TC 5, and the average pressure reading between 14:10 and 14:30. The pressure appears to spike immediately after a temperature drop is measured in the thermocouples. The phenomenon is apparent in both the two large pressure pulsations, as well as in the smaller pressure oscillations.

The surface thermocouple measurements, along with their respective steam temperature measurements, are plotted in Figure 22 to Figure 24. A summary of the results is presented in Table 2. This was done to approximate the types of flow that were occurring in the coil turns.

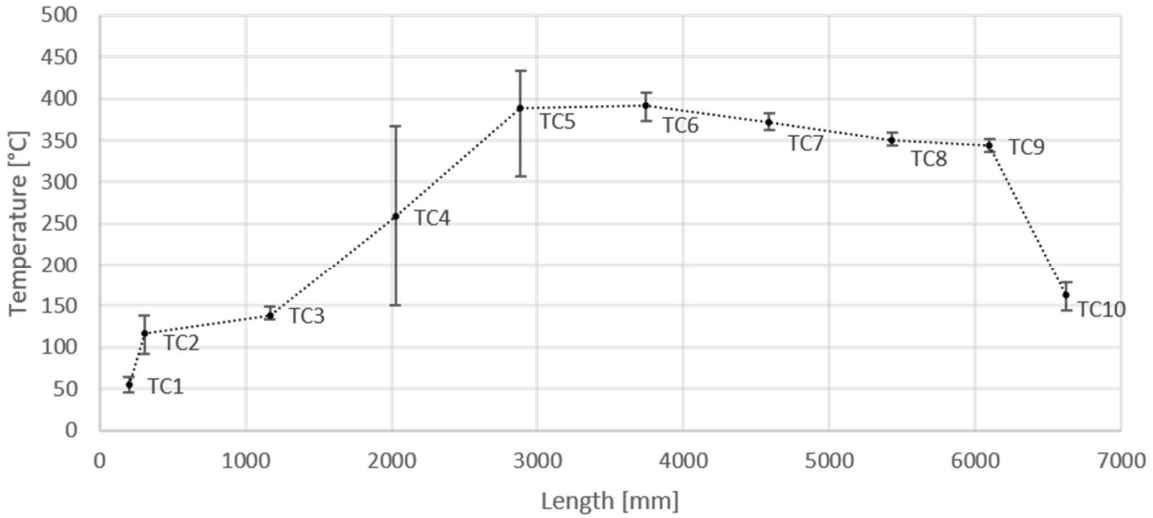

Figure 20: Time-averaged steam temperature readings along the length of the coil.

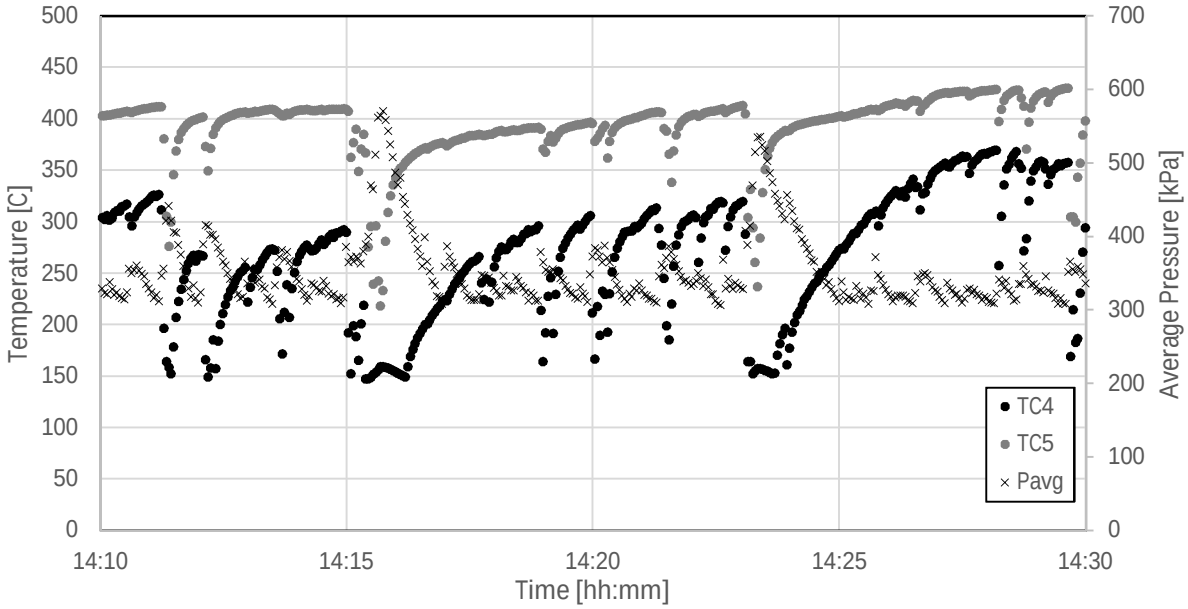

Figure 21: Temperature and pressure results between 14:10 and 14:30.

Considering the surface temperature measurements in the third coil turn, illustrated in Figure 22, it may be observed that the inner coil wall temperature of TC 3i is notably larger than the outer coil wall temperature of TC 3o. A temperature difference of 89 °C between the inner

and outer walls is observable from the averages in Table 2. The outer coil wall temperature is comparable to the fluid temperature of TC 3, which is at saturation temperature.

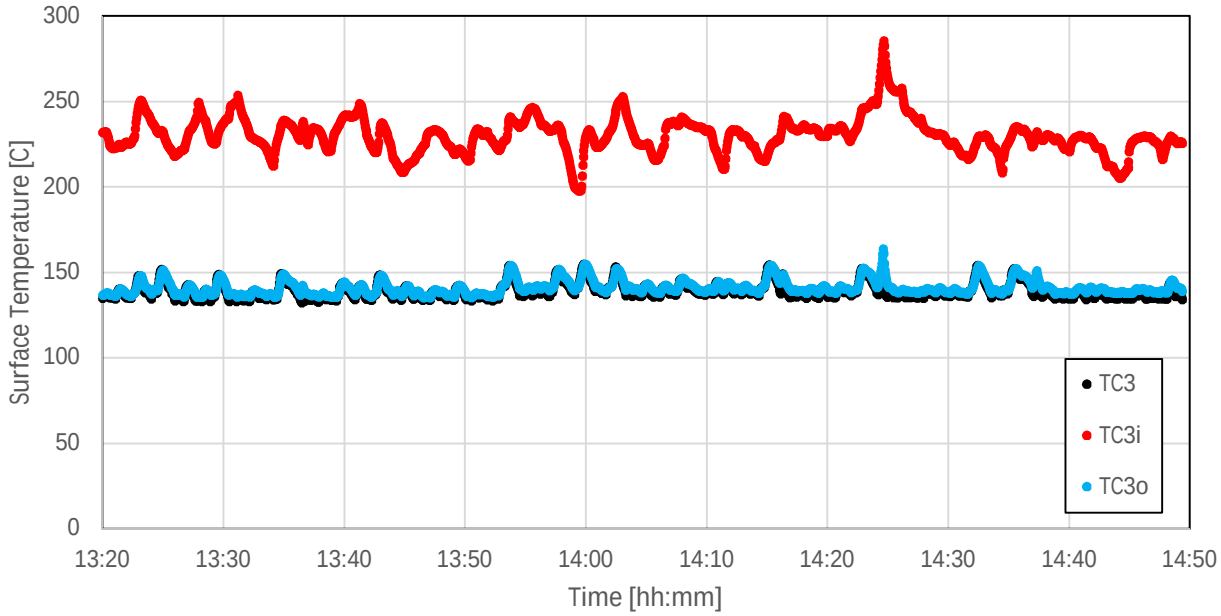

Figure 22: Steam and wall temperature measurements taken for the third coil turn.

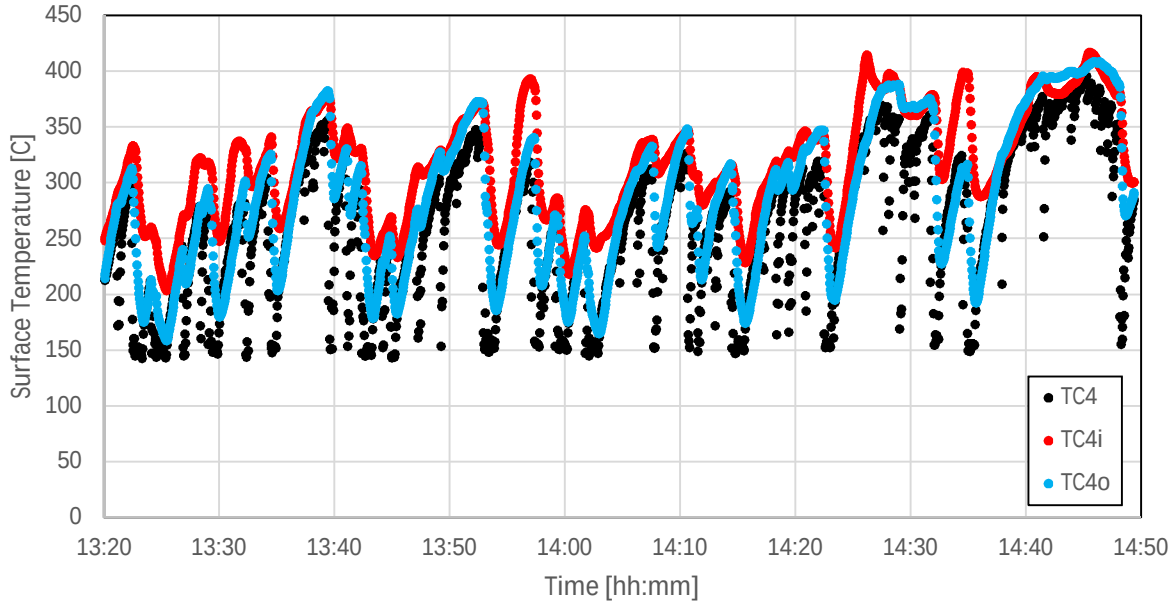

Figure 23: Steam and wall temperature measurements taken for the fifth coil turn.

The temperatures in the fifth coil turn follow an erratic oscillation with the steam temperature frequently dropping towards saturation temperature and then spiking towards the measured wall temperatures. In certain instances, such as at 13:40, the temperature difference between

the inner coil wall and the steam is roughly 180 °C. The temperatures of the inner and outer walls of the coil are grouped notably closer together when compared to the temperature in the third coil turn, and their average temperature difference is 30 °C.

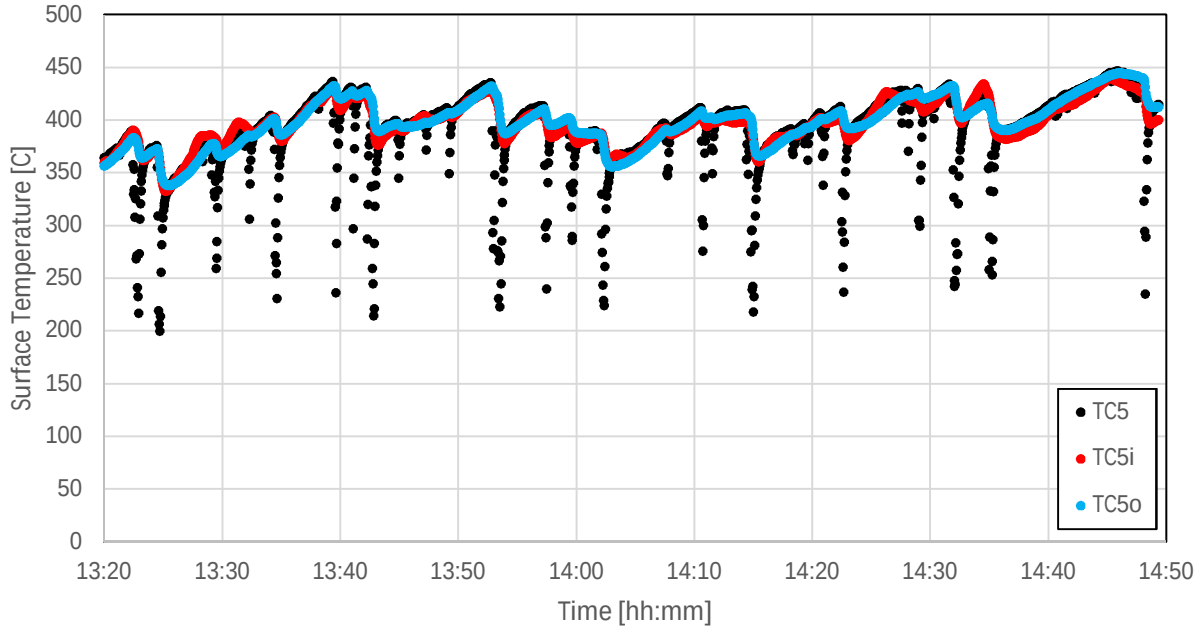

Figure 24: Steam and wall temperature measurements taken for the seventh coil turn.

Table 2: Time-averaged and statistical summary of the surface thermocouple measurements during the testing period

Thermocouples		Average (°C)	Maximum (°C)	Minimum (°C)	Standard deviation (°C)
TC 3	Inner	230.2	285.4	197.7	10.6
	Fluid	139.0	154.4	132.2	4.4
	Outer	140.7	163.4	135.2	4.2
TC 4	Inner	315.9	416.7	203.8	50.1
	Fluid	258.1	395.7	139.7	68.7
	Outer	286.1	408.4	158.5	67.1
TC 5	Inner	396.5	440.2	333.0	21.0
	Fluid	389.1	446.8	199.6	38.6
	Outer	397.6	444.7	338.4	23.4

By the seventh coil turn, the oscillations in the inner and outer coil wall temperatures had begun to stabilise at average temperatures of 396 and 398 °C, respectively. There is now a negative difference of 2 °C between the inner and outer coil wall temperatures, which is counter-intuitive since the inner wall is still receiving radiative heat from the concentrated

solar radiation. However, the difference is so small that one could assume that the two walls are now uniform in temperature. There are still instances where the steam temperature drops towards saturation temperature. The maximum temperature difference between the steam and the walls is measured to be 177 °C.

5. Discussion

5.1. Flow within the coil

The pressure oscillations were determined to come from the rapid expansion of steam since the pressure spikes occurred directly at the time that TC 3 and TC 5 measured a sudden drop in temperature towards saturation (see Figure 21). This suggests that a slug type flow was occurring. As a new slug of liquid passes into the fourth coil turn, a temperature drop towards saturation temperature is measured. As the liquid comes into contact with the higher temperature walls, it rapidly expands into steam. This rapid expansion causes a spike in pressure, which, in turn, closes the check valve at the inlet. Thus, the only way for the flow to escape is through the needle valve at the outlet, which is set at a constant aperture. Studies investigating two-phase flow boiling instabilities show that pressure oscillations accommodate thermal oscillations in boiling flow and the maximum pressure lags the maximum temperature during each oscillation as was observed in the current study [48-50].

The temperature oscillations that are measured between TC 2 and TC 8, in Figure 19, suggest that this coil region is dealing with intermittent two-phase flow [48, 51]. A similar analysis was performed with a conductivity probe in Zhu et al. [25]. At TC 2, it is suspected that bubbly flow is occurring, where the fluid temperature spikes towards saturation temperature as the water begins to boil. A vapour bubble encapsulates the thermocouple junction, and then suddenly drops as the junction comes into contact with the fluid again. The oscillations become more erratic after TC 3 and then subside by TC 6, which suggests that superheated steam was being produced by the eleventh coil turn and the flow was mostly single phase.

Based on the observations made of the surface temperature readings in Figure 22 to Figure 24 and the studies on flow patterns in helically coiled tubes conducted by Zhu et al. [25] and Cui et al. [24], the flow patterns at the three coil turns may be estimated (see Figure 25 to Figure 27). In the third coil turn, a temperature difference of 89 °C was observed between the

average temperatures of the inner and outer walls. The temperature of the fluid was comparable to that of the outer wall. This suggests that dryout was initiated before this point and the coil turn mostly experienced stratified flow where expanded steam passed through the inner coil wall nearest to the helical axis. Saturated liquid was in contact with most of the outer wall inside the coil tube and enveloped the thermocouple junction. The flow stratification is suspected to be a result of the rapid expansion of steam on the inner side of the coil tube due to the incidence of solar radiation. Since the flow rate is so low, at 0.2938 g/s, it is suspected that centrifugal forces play a negligible role in this stratification. This would result in the notable temperature difference that was observed.

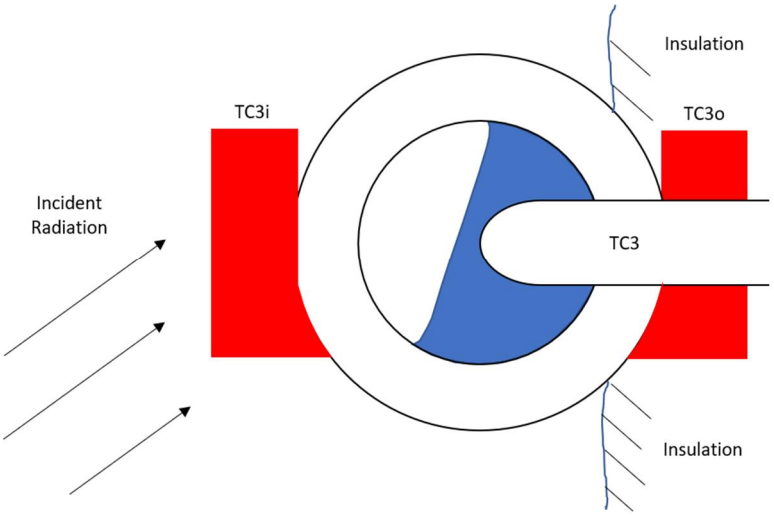

Figure 25: Cross-section of the third coil turn during the testing period.

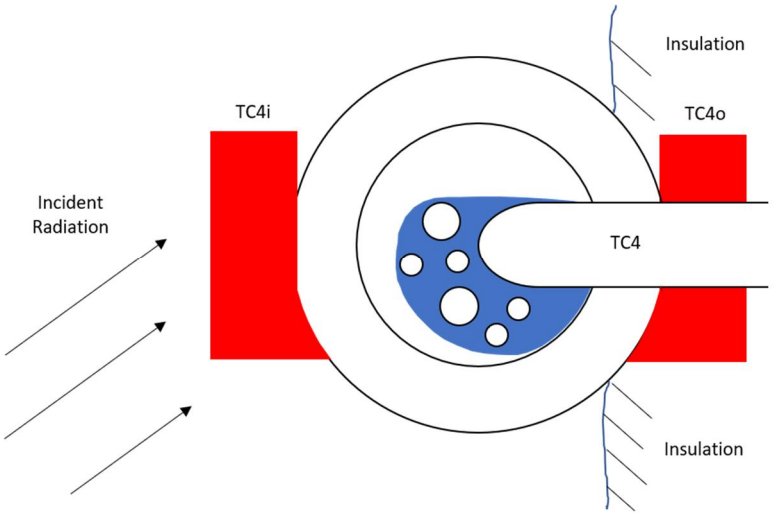

Figure 26: Cross-section of the fifth coil turn during the testing period.

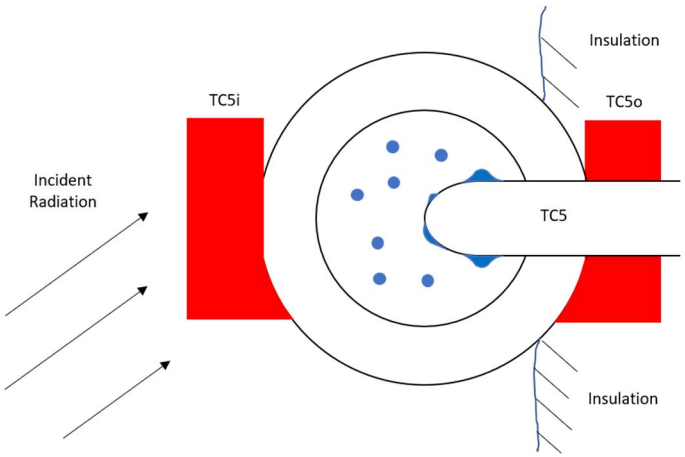

Figure 27: Cross-section of the seventh coil turn during the testing period.

The fifth coil turn had an interesting phenomenon, where the steam temperature measurements oscillated between saturation and the inner coil wall temperature of TC 4i. Based on this observation, it is estimated that intermittent, slug-type flow was occurring. During such an oscillation, the drop in fluid temperature suggests that a slug of saturated liquid is in contact with the insertion thermocouple junction. The temperature difference between the saturated liquid and the inner wall of the coil tube was observed to be greater than 120 °C in certain instances. This suggests that Leidenfrost boiling had been initiated by this point [43]. Therefore, the flow regime illustrates the liquid slug not being in contact with the walls of the coil tube.

By the seventh coil turn, it was suspected that Leidenfrost boiling had become fully initiated with both the inner and outer coil tube walls having a temperature difference of 177 °C compared to the saturated liquid slugs. Thus, Figure 27 illustrates a flow regime where droplet entrainment occurs and wet steam accumulates on the insertion thermocouple junction but does not come into contact with the coil tube walls due to the Leidenfrost effect. This explains the sudden drop in steam temperature, while the tube wall temperatures experience a negligible effect.

5.2. First-law efficiency

The thermal efficiencies of the solar receiver and the solar collector were determined based on Equations (7) and (8), and are plotted in Figure 28 and Figure 29. The inlet temperature to the receiver was taken to be at TC 1, while the outlet of the receiver was considered to be at TC 9 since TC 10 was not insulated. The slight decrement in temperature between TC 7 and

TC 9 is considered to be the result of the intercepted radiation only being incident on the first seven coil turns, as was observed in Figure 15. The notable temperature drop between TC 9 and TC 10 is considered to be due to convection heat loss from the process piping outside the receiver cavity. The slight decrement in the DNI increased both thermal efficiencies since the inlet and outlet steam temperatures were effectively constant over the 91-minute period. Intermittency of the DNI could be mitigated using TES solutions. Based on the work of Alva et al. [10], high temperature operating conditions greater than 250 °C can incorporate latent heat TES since melting points of salts and metals are reached. Suitable TES candidates are pure zinc [52] and aluminium-magnesium-zinc alloys [53].

Considering the reflectivity of the reflector to be 97% and the intercept factor at the 135-mm-diameter aperture to be 87%, the collector was able to produce an average of 861 W from the incident solar radiation of 2 044 W. The average receiver and collector efficiencies were 50 and 42%, respectively. This meant that, of the total solar radiation incident on the solar dish facets, 42% could be captured through the coils. Of the total concentrated radiation that was intercepted through the receiver aperture, 50% could be captured through the coils.

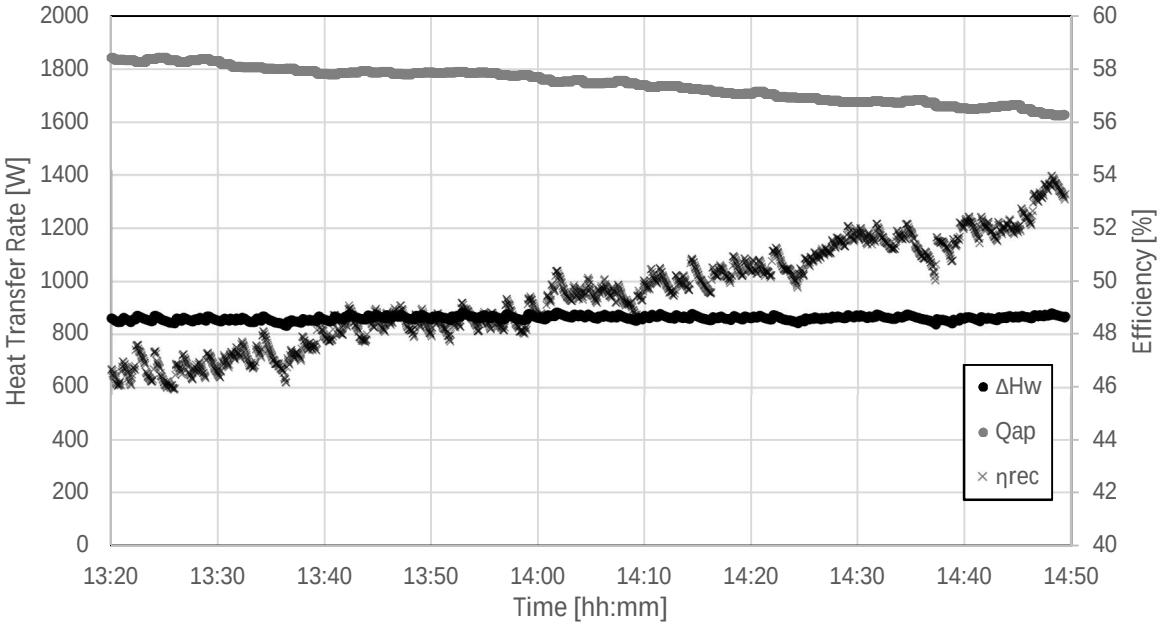

Figure 28: Heat transfer rate to the steam and receiver's first-law efficiency during testing.

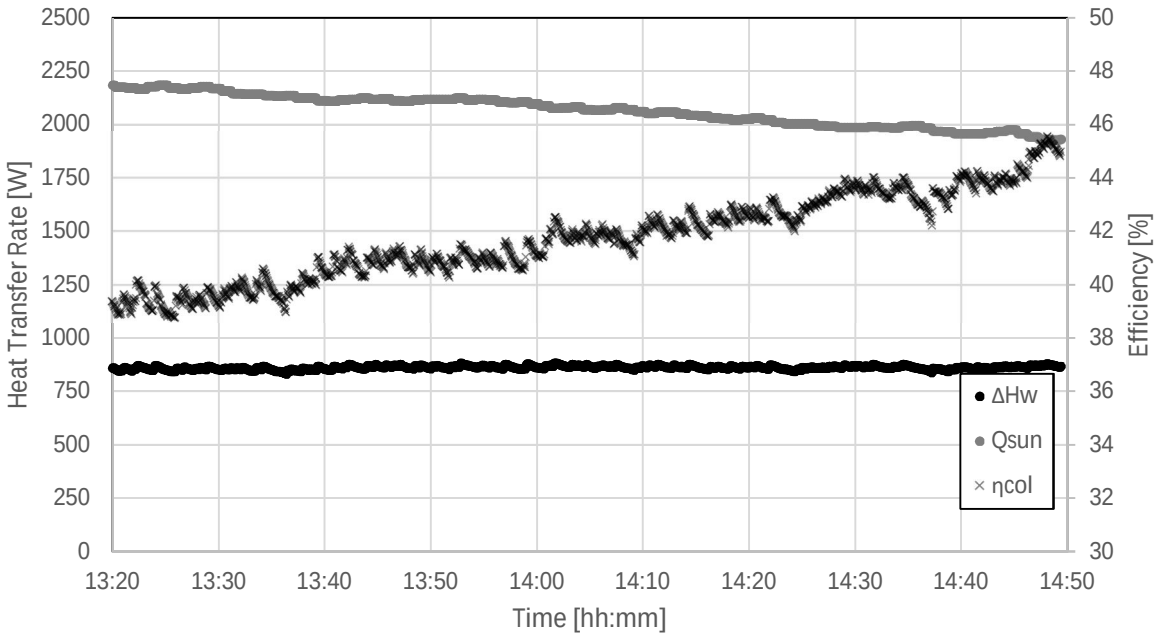

Figure 29: Heat transfer rate to the steam and collector's first-law efficiency during testing.

To facilitate a comparison between the current work and previous experimental research, the results obtained are compared with different small-scale solar collectors. Zhu et al. [54] investigated a 44 m^2 parabolic dish with a cavity receiver using air as the working fluid and obtained a steady-state receiver efficiency of approximately 60%. Pavlovic et al. [15] investigated the performance of a 10.29 m^2 parabolic dish with a corrugated spiral absorber using water as the heat transfer fluid. The analysis obtained a 34% collector efficiency at steady state. Loni et al. [19] analysed the performance of a 2.84 m^2 parabolic dish with two different cavity receiver shapes using Behran thermal oil as the heat transfer fluid and obtained steady-state collector efficiencies of between 56% and 66%. These efficiencies are comparable to the results obtained in the current work; however, the current work investigated micro-scale direct steam generation using a multifaceted 2.7 m^2 solar dish.

5.3. Heat loss

According to the results in Figure 28 and Figure 29, the thermal losses within the cavity contribute notably to the efficiency of the solar collector and the receiver. Since the intercepted heat and the captured heat are known, the heat loss from the receiver was determined using Equation (3). This is plotted in Figure 30. The average heat loss rate from the receiver was determined to be 865 W over the testing period. Based on the heat loss model presented in

Section 3.3, the heat loss was broken down into its fundamental components to aid in characterising the performance of the receiver.

The solar collector's elevation angle was measured to be 40° on average during the testing period. The average ambient temperature was measured to be 29.6 °C during the testing period, with a measured average wind velocity of 1.7 m/s. The convection heat loss was determined considering the aperture diameter of the receiver to be 135 mm with the inner diameter of the cavity being approximately 150 mm and the average surface temperature of the cavity being 315.8 °C. The results are presented in Table 3.

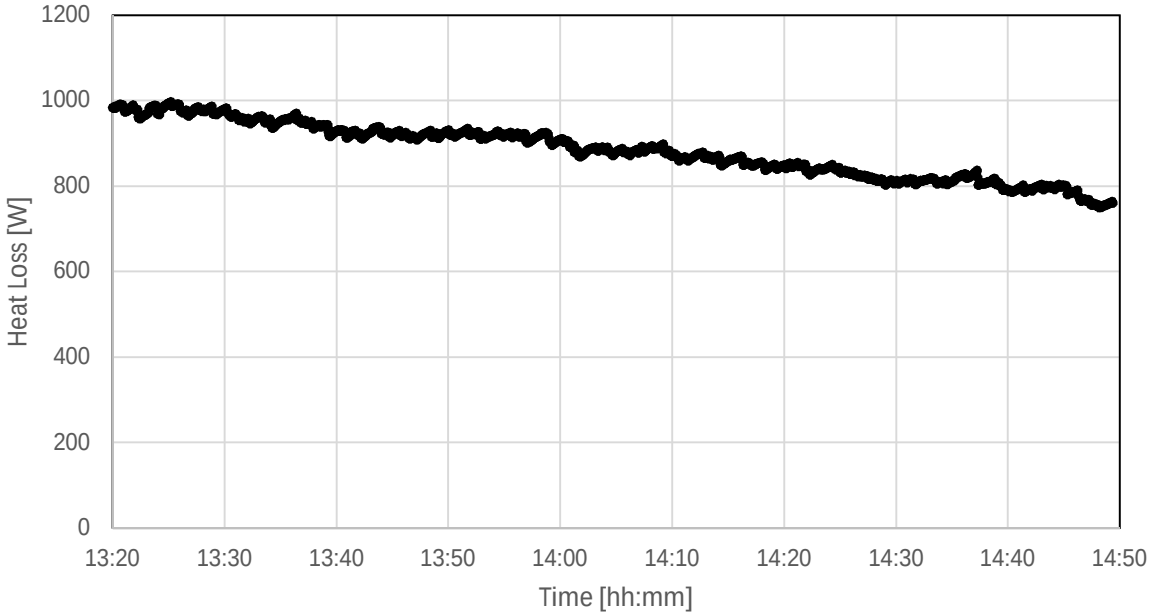

Figure 30: Heat loss from the receiver during testing.

Table 3: Results of the Nusselt number calculation for natural convection heat loss through the receiver aperture

Parameter	Value	Units
Characteristic length (L_c)	0.2	m
Property temperature (T_{prop})	302.79	K
Grashof number (Gr)	2.11e8	-
Prandtl number (Pr)	0.71	-
Nusselt number ($Nu_{natural}$)	25.54	-
Convection coefficient ($\bar{h}_{natural}$)	3.40	W/m^{2}K

Table 4: Results of the conduction heat loss analysis

Description, symbol, and unit	Value					
	Front	Back	Left	Right	Top	Bottom
Conduction heat loss						
Insulation surface temperature, $T_{ins,out}$ (K)	358.1	333.4	350.8	350.8	322.9	335.8
Film temperature, T_f (K)	330.5	318.1	326.8	326.8	312.8	319.3
Surface area (inner cavity), $A_{ins,in}$ (m^2)	0.04	0.04	0.04	0.04	0.02	0.01
Surface area (outer cavity), $A_{ins,out}$ (m^2)	0.07	0.07	0.08	0.08	0.05	0.02
Insulation thickness, t_{ins} (m)	0.025	0.05	0.025	0.025	0.05	0.025
Forced convection						
Characteristic length (forced), $L_{c,forced,i}$ (m)	0.28	0.28	0.28	0.28	0.2	0.2
Grashof number, Gr	2.01E+08	2.39E+08	2.11E+08	2.11E+08	9.10E+07	8.29E+07
Reynolds number, Re	2.21E+04	2.36E+04	2.25E+04	2.25E+04	1.72E+04	1.66E+04
Nusselt number, $Nu_{forced,i}$	82.3	85.7	83.2	83.2	77.6	76.1
Convection coefficient (forced), $\bar{h}_{forced,i}$ (W/m^2K)	8.32	8.39	8.34	8.34	10.6	10.6
Natural convection						
Elevation angle, θ (deg)	40	40	90	90	60	60
Angle of inclination, φ (deg)	50	50	0	0	30	30
Characteristic Rayleigh number, $GrcPr$	7.22E+07	-	-	-	3.00E+08	-
Characteristic length (natural), $L_{c,natural,i}$ (m)	0.37	0.37	0.37	0.37	0.25	0.25
Grashof number, Gr	1.67E+08	1.10E+08	1.52E+08	1.52E+08	2.49E+07	3.74E+07
Rayleigh number, Ra	1.17E+08	7.72E+07	1.07E+08	1.07E+08	1.76E+07	2.64E+07
Nusselt number, $Nu_{natural,i}$	55.7	47.0	57.0	57.0	17.9	38.7
Convection coefficient (natural), $\bar{h}_{natural,i}$	4.37	3.57	4.42	4.42	1.96	4.30
Total heat loss						
Combined Nusselt number, $Nu_{comb,i}$	87.8	88.5	89.0	89.0	77.7	78.1
Combined characteristic length, $L_{c,comb,i}$	0.30	0.29	0.30	0.30	0.20	0.20
Combined convection coefficient, $\bar{h}_{comb,i}$	8.38	8.41	8.41	8.41	10.6	10.6
Conduction heat loss rate, $\dot{Q}_{cond,loss}$	32.1	17.8	33.2	33.2	9.58	6.63

Table 5: Heat loss breakdown.

Description	Symbol	Heat loss rate (W)	Relative heat loss
Convection heat loss	$\dot{\boldsymbol{Q}}_{\boldsymbol{loss,conv}}$	382	45%
Natural convection loss through aperture	$\dot{Q}_{conv,natural}$	127	
Forced convection loss through aperture	$\dot{Q}_{conv,forced}$	255	
Radiation heat loss	$\dot{\boldsymbol{Q}}_{\boldsymbol{loss,rad}}$	325	39%
Radiation emitted from the coils	$\dot{Q}_{rad,emit}$	65	
Radiation reflected from the cavity	$\dot{Q}_{rad,ref}$	260	
Conduction heat loss	$\dot{\boldsymbol{Q}}_{\boldsymbol{loss,cond}}$	132	16%
Conduction loss from the front of the cavity	$\dot{Q}_{cond,front}$	32	
Conduction loss from the back of the cavity	$\dot{Q}_{cond,back}$	18	
Conduction loss from the left of the cavity	$\dot{Q}_{cond,left}$	33	
Conduction loss from the right of the cavity	$\dot{Q}_{cond,right}$	33	
Conduction loss from the top of the cavity	$\dot{Q}_{cond,top}$	10	
Conduction loss from the bottom of the cavity	$\dot{Q}_{cond,bottom}$	7	
Total theoretical heat loss	$\dot{\boldsymbol{Q}}^{*}_{\boldsymbol{loss}}$	839	100%
Experimental heat loss	$\dot{\boldsymbol{Q}}_{\boldsymbol{loss}}$	865	-

Since the wind speeds were below 4.5 m/s, the forced convection heat transfer coefficient was approximated to be twice that of the natural convection heat transfer coefficient, based on the work of Harris and Lenz [42]. The coil tubes were considered to have the optical properties of thermally oxidised stainless steel (oxidised for 10 minutes at 1 043 K under atmospheric conditions), which has a solar absorptivity of 0.85 [55]. The emissivity of the coil tubes was estimated using the work of Cengel and Ghajar [43]. For lightly oxidised stainless steel at 326.9 °C, which is comparable to the surface temperature of the coil tube in the experimental cavity, the emissivity was reported to be 0.3. At the average surface temperature of 315.8 °C, the total reflected radiation and emitted radiation were determined to be 262.4 W and 65.3 W, respectively. Considering the measured ambient temperature, wind speed and taking the inner cavity insulation temperature to equal the average coil surface temperature, the conduction heat losses through all sides of the cavity were calculated. A summary of the solution to the conduction heat loss analysis is presented in Table 4.

The heat loss modes are summarised in Table 5 and Figure 31. The total heat loss, using the analytical model, was estimated to be 839 W, while the average experimental heat loss was

determined to be 865 W. When comparing the heat loss model to the experimental results, the heat loss model predicts the experimental steady-state heat loss rate with an accuracy of approximately 97%. It is evident from the summary that convection heat loss is the dominant mode present for the given receiver design, with 45% relative heat loss. It is also evident that 84% of the heat loss is through the aperture of the cavity. It is suspected that the concentrated radiation only being incident on the first seven coil turns had a notable effect on the radiation heat loss through the aperture. An optimization study is recommended for future work to determine the relationship between the incident radiation distribution on the coil surface and the radiative heat loss from the receiver cavity. Improving the accuracy of the faceted reflector would further aid in reducing the heat losses from the receiver aperture by reducing the required aperture size.

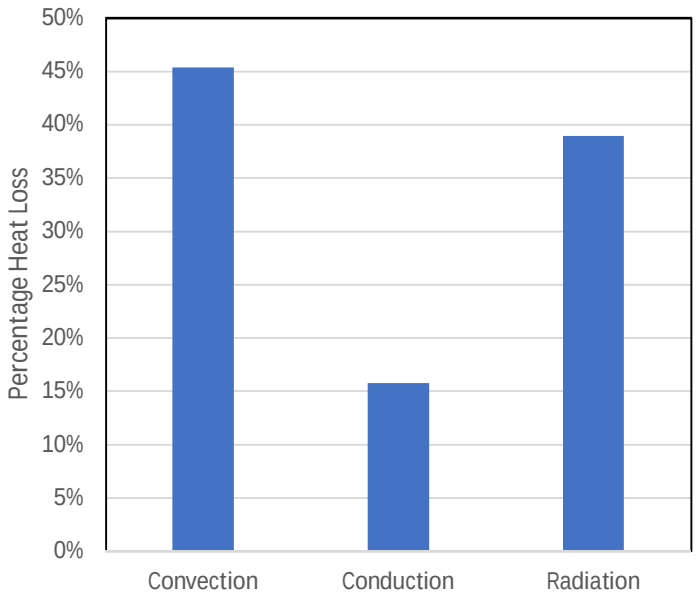

Figure 31: Relative heat loss from the receiver.

5.4. Second-law analysis

An exergy analysis was performed on the receiver where the second-law efficiency was determined for the steady-state period. The analysis provides additional information with regard to the potential of the solar collector to generate useful work and it highlights key aspects to be considered when optimising the performance of the system. The results were plotted in Figure 32. The exergy of the steam at the inlet and outlet of the receiver was determined from Equation (10). The available work from the intercepted radiation was

determined from Equation (12). The ambient temperature and ambient pressure measurements were taken using the SOLYS 2 Sun Tracker [34]. The sun's temperature was taken to be 5 762 K [43]. The average second-law efficiency was determined to be 12% over the testing period.

It is important to consider the irreversibility breakdown of the test facility to define the main contributors of irreversibility in the system. Figure 33 illustrates the different contributors of irreversibility that are considered in the current study.

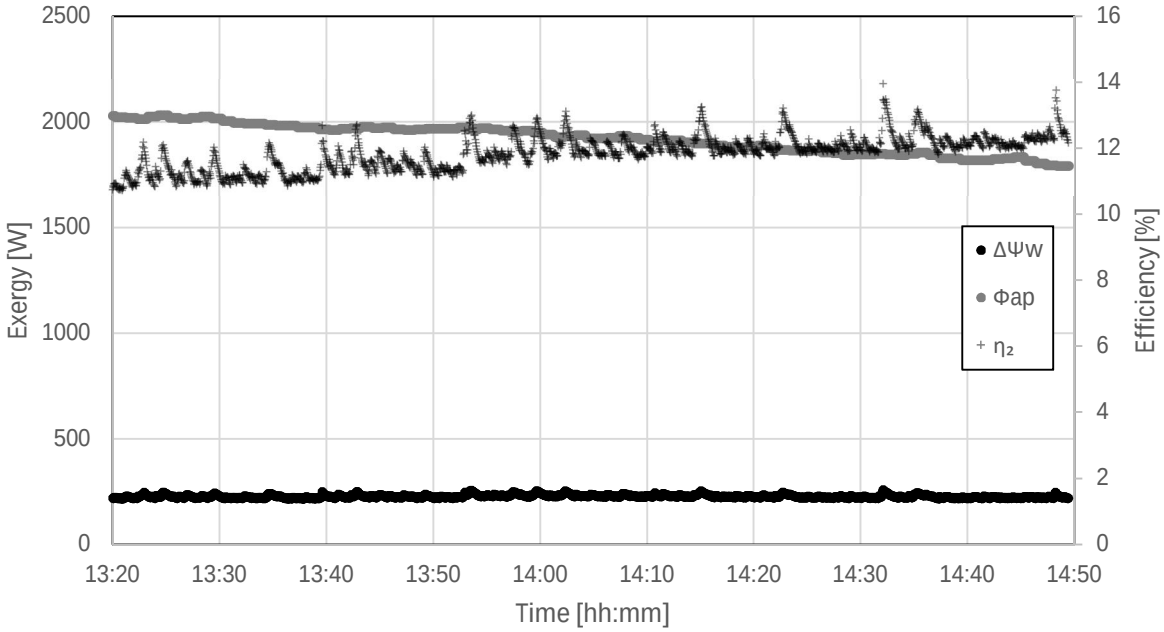

Figure 32: Second-law analysis of the solar receiver for the steady-state period.

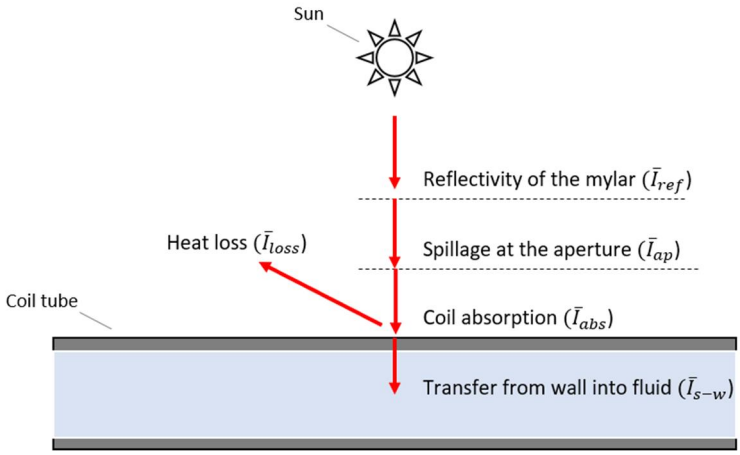

Figure 33: Contributors to irreversibility with the solar collector.

The analysis can be further broken down into first-law heat transfer components and their respective second-law components, as presented in Figure 34. As is evident in Figure 34a, the reflected radiation heat loss component is handled separately from the total heat loss from the receiver coil. This is because of the available work of the reflected component is determined using the sun as the reference temperature, whereas the available work of the convection and emission heat loss is determined using the tube wall temperature as the reference. The heat that is absorbed by the coil also represents the component that is eventually absorbed by the working fluid. The exergy terms were determined using the second-law analysis model and are presented in Table 6, along with their respective equations used to determine the values.

Table 6: Summary of the second-law exergy components

Exergy components	Symbol	Surface temperature ($\boldsymbol{T_s}$)(K)	Heat transfer rate ($\dot{\boldsymbol{Q}}$)(W)	Exergy (W)	Equation reference
Available work from the sun	Φ_{sun}	5 762	2 045	1 902	(12)
Available work from the reflected radiation	Φ_{ref}	5 762	1 984	1 845	(12)
Available work intercepting the aperture	Φ_{ap}	5 762	1 726	1 605	(12)
Available work being reflected by the coil and lost through the aperture	$\Phi_{ap,ref}$	5 762	260	241	(12)
Available work being absorbed by the coil tube wall	Φ_{abs}	589	861	418	(11)
Available work being lost by the receiver	Φ_{loss}	589	606	294	(11)
Change in exergy of the steam	$\Delta\Psi_{\mathrm{w}}$	-	-	227	(10)

The total irreversibility of the solar collector was found to be 1 675 W using Equation (14), with $\Delta\Psi_{\mathrm{w}}$ = 227 W and Φ_{sun} = 1 902 W. The irreversibility contributions were determined by considering the specific components within the solar collector as discretised control volumes and defining the exergy transfer in and out of each control volume. The equations used to calculate the irreversibilities are presented in equations (33) to (38). The results are presented in Table 7.

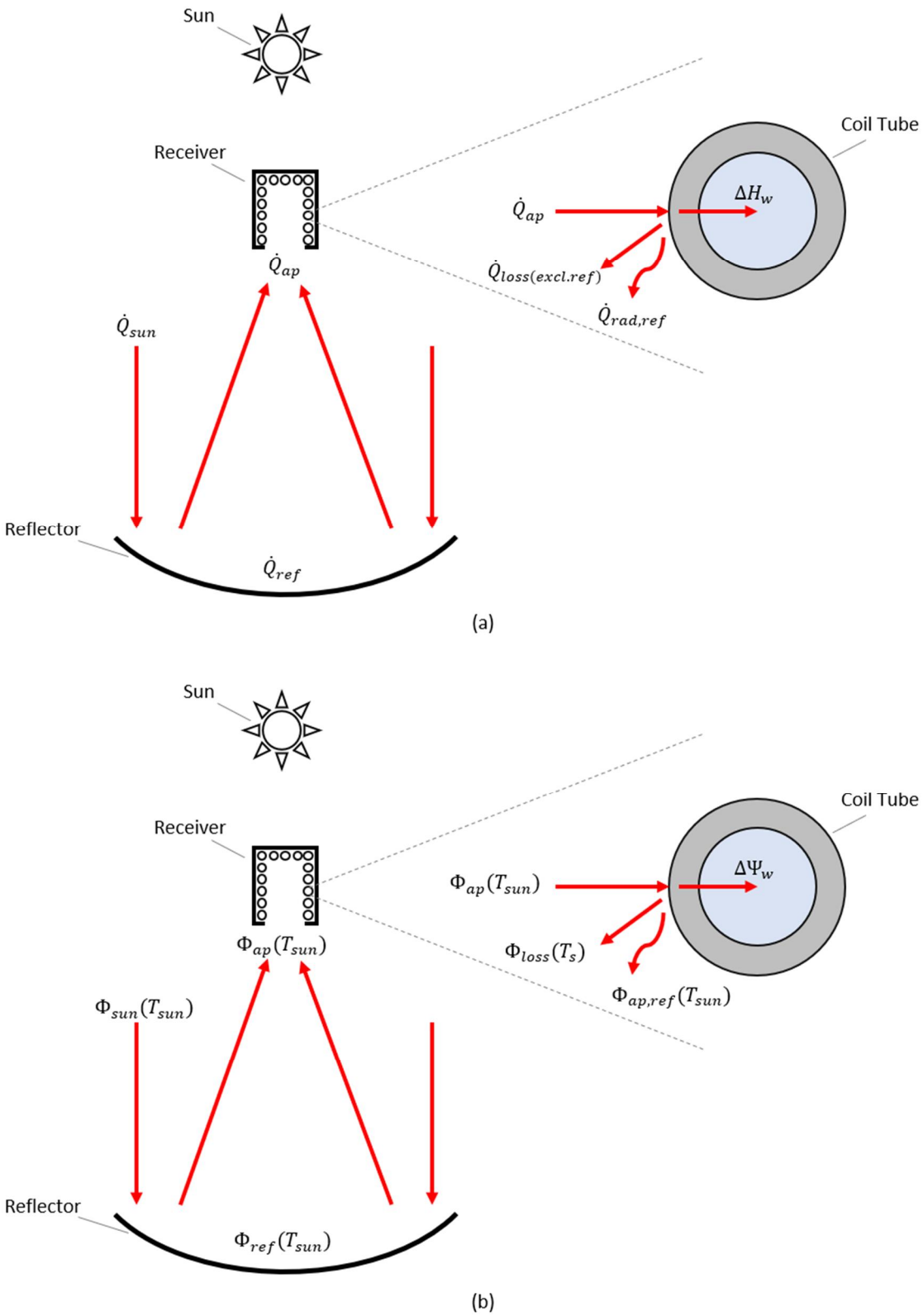

Figure 34: (a): First-law energy components; and (b) second-law exergy components.

$$\bar{I}_{ref} = -1 \times (\Phi_{\text{ref}} - \Phi_{sun}) \quad (33)$$

$$\bar{I}_{ap} = -1 \times (\Phi_{ap} - \Phi_{ref}) \quad (34)$$

$$\bar{I}_{ap,ref} = \Phi_{ap,ref} \quad (35)$$

$$\bar{I}_{abs} = -1 \times (\Phi_{abs} + \Phi_{ap,ref} + \Phi_{loss} - \Phi_{ap}) \quad (36)$$

$$\bar{I}_{loss} = \Phi_{loss} \quad (37)$$

$$\bar{I}_{s-w} = -1 \times (\Delta\Psi_{\text{w}} - \Phi_{abs}) \quad (38)$$

Table 7: Irreversibility breakdown for the solar collector

Irreversibility contributors	Symbol	Irreversibility (W)	Contribution
The reflectivity of the Mylar sheet	$\bar{I}_{ref}$	57	3%
Spillage at the aperture	$\bar{I}_{ap}$	240	14%
Reflected radiation loss from the coil	$\bar{I}_{ap,ref}$	249	15%
Coil absorption	$\bar{I}_{abs}$	644	38%
Transfer from tube wall to working fluid	$\bar{I}_{s-w}$	191	11%
Thermal heat loss	$\bar{I}_{loss}$	294	18%
Total breakdown	$\boldsymbol{\bar{I}_{total}}$	1 675	100%

It is evident in Table 7 that, although the loss components contribute 32% of the total irreversibility of the solar collector, the heat absorption in the coil makes the largest contribution to the total irreversibility, at a 38% contribution. This is due to the significant difference in surface temperature between the sun and the receiver coil. This irreversibility can be addressed by shifting the entire power cycle up in pressure and temperature. However, this will conversely increase the heat loss irreversibility that is present.

An optimum set of operating conditions can thus be determined with enough empirical information. A parametric analysis, where the solar collector is analysed for varying operating conditions, is thus recommended for future work. The heat loss irreversibility can be addressed by optimising the collector design, as mentioned in Section 5.3.

6. Conclusions

This research presents an experimental investigation into the performance of a micro-scale, solar thermal direct steam generator using a low-cost solar collector (a stretched-membrane, faceted dish and helical coil solar receiver). During the testing period, steady inlet and outlet steam temperatures were achieved with water running through the receiver at 0.2938 g/s at a supply pressure of 3 bar. The inlet temperature was kept steady at 54 °C, and the outlet temperature was kept steady at 343.12 °C. With an average solar irradiance of 757 W/m^2 measured over the testing period and a reflector incident area of 2.70 m^2, the solar collector was able to capture 865 W of heat in the working fluid. Flow boiling initiated at the first coil turn and expanded rapidly to stratified flow by the third coil turn. The Leidenfrost effect was observable by the fifth coil turn with temperature oscillations suggesting slug type flow. By the seventh coil turn, the Leidenfrost effect appeared to produce droplet entrainment. The thermal efficiency of the collector was thus determined to be 42% and the thermal efficiency of the receiver was 50%, with room for improvement. According to the experimental results, a total heat loss rate of 865 W was determined. A heat loss model was developed that could predict the steady-state heat loss rate with an accuracy of 97%. According to the heat loss model, the main contributors to the heat loss from the receiver were the convection and radiation heat losses (emitted and reflected) through the aperture. These components formed 84% of the total heat loss in the receiver. The average second-law efficiency of the solar collector was determined to be 12% over the testing period. From the second-law analysis, it was found that the large temperature difference between the surface temperature of the sun and the surface temperature of the coils caused the largest irreversibility to occur. Irreversibility from the incident solar radiation heat absorption into the receiver coil accounted for 38% of the total irreversibility.

The study has highlighted important design aspects that became evident and recommendations are made for future work:

- Pressure oscillations that occurred during testing limited the operating pressure of the system. A pressure control valve should rather be used to control the flow at the outlet of the test section rather than a ball valve.

- Water was selected as a working fluid for the current study due to its availability and the lack of research available. However, organic alternatives may be more suitable at the given scale of power generation, particularly with regard to compatibility with the low temperature operating conditions of volumetric expander technology.
- The incident radiation distribution on the receiver coil directly affects the heat loss from the cavity aperture. A parametric investigation of reflector shape and cavity aspect ratio should be conducted to minimise heat losses at the cavity aperture. It is expected that reflected radiation losses can be significantly decreased by optimising the incident radiation distribution along the receiver coil.
- An optimum set of operating conditions could be determined for the solar collector by comparing the irreversibility of coil absorption and the irreversibility of heat loss for a given change in surface temperature. This can be achieved through parametric experimental analysis at different operating conditions.

Acknowledgements

This work is based on research supported by the National Research Foundation (NRF) of South Africa (Grant Number 109311), the Technology Innovation Agency (TIA) of South Africa and the Department of Science and Innovation (DSI). Opinions expressed and conclusions arrived at are those of the author and are not necessarily to be attributed to the NRF, TIA or DSI. The authors also acknowledge the South African Universities Radiometric Network (SAURAN) for providing weather data.

Appendix A: Uncertainty analysis

The uncertainties associated with the measurement devices used in the current research were determined according to the guidelines presented in the ISO/IEC Guide 98-3:2008 [56]. The standard uncertainty is statistically representative of 1 standard deviation from the mean, assuming a normal distribution. The standard uncertainties of the measurement devices were either determined from calibration or the manufacturer's equipment specifications. Considering the calibration curves of the thermocouples, pressure transmitters and the load cell, their standard uncertainties were determined by taking the root sum of squares of the

reference standard uncertainty $\delta(x_{ref})$ and the calibration variance b_i as presented in Equation (39).

$$\delta(x_i) = \sqrt{b_i^2 + \delta^2(x_{ref})} \tag{39}$$

The total uncertainty accounts for 2 standard deviations from the mean, or a 95% confidence level, and is referred to as the measurement uncertainty or expanded uncertainty in the current research. The measurement uncertainties associated with the primary measurement devices are presented in Table 8.

Table 8: Summary of measurement uncertainties

Parameter	Measurement uncertainty	Relative uncertainty
Temperature (K)		
TC 1	3.05	5.63%
TC 2	2.66	2.27%
TC 3	3.10	2.23%
TC 4	2.43	0.94%
TC 5	2.69	0.69%
TC 6	2.51	0.64%
TC 7	2.66	0.71%
TC 8	2.58	0.74%
TC 9	2.79	0.81%
TC 10	2.50	1.53%
T_∞	0.85	0.28%
Pressure (kPa)		
$P1$	0.78	0.23%
$P2$	5.30	1.51%
P_∞	0.22	0.29%
Mass (kg)		
m_w	0.01	-
Length (m)		
L	0.002	-
DNI (W/m^2)		
I_{sun}, [35]	30	2.00 %
Dish reflectivity (-)		
η_{ref}, [33]	0.03	3.22%
Flux mapping (-)		
η_{LFM}, [57]	-	3.00%
η_{camera}, [58]	-	7.00%

Using the method of error propagation, the combined standard uncertainties in Equations (40) to (48) were determined for the fundamental output parameters in the research. This was done by considering the component standard uncertainty of the measurements and the sensitivity associated with each. The combined standard uncertainties were then expanded to account for a 95% confidence level. The results, along with the associated equations, are presented in Table 9.

The analysis showed that the prominent propagator of uncertainty came from the intercept factor that was determined from the lunar flux mapping analysis. The uncertainties involved in this analysis influenced the results of the thermal analysis, particularly in the calculation of the intercepted radiation at the aperture. The maximum uncertainty came from the first-law and second-law efficiencies of the receiver with a relative uncertainty of 10 and 13%, respectively.

Table 9: Expanded uncertainty for fundamental output parameters

Parameter (units)	Symbol	Expanded uncertainty	Relative uncertainty
Incident dish area (m^2)	A_{dish}	0.04	1.66%
$\delta(A_{dish}) = [(6\pi\bar{B})^2\,\delta^2(\overline{A^*}) + (6\pi\overline{A^*})^2\delta^2(\bar{B})]^{0.5}$ (40)			
Intercept factor (-)	IF	0.08	8.79%
$\delta(IF) \approx IF \times \left[\left(\frac{\delta\eta_{camera}}{\eta_{camera}}\right)^2 + \left(\frac{\delta\eta_{LFM}}{\eta_{LFM}}\right)^2\right]^{0.5}$ (41)			
Mass flow rate (kg/s)	$\dot{m}_w$	2.92E-06	0.99%
$\delta(\dot{m}_w) = \left[\left(-\frac{1}{\Delta t}\right)^2 \times \delta^2(m_{w,1}) + \left(\frac{1}{\Delta t}\right)^2 \times \delta^2(m_{w,2}) + \left(\frac{m_{w,2} - m_{w,1}}{(\Delta t)^2}\right)^2 \times \delta^2(\Delta t)\right]^{0.5}$ (42)			
Captured heat (W)	ΔH_w	16.96	1.97%
$\delta(\Delta H_w) = [(h_{in} - h_{out})^2 \times \delta^2(\dot{m}_w) + (\dot{m}_w)^2 \times \delta^2(h_{in}) + (-\dot{m}_w)^2 \times \delta^2(h_{out})]^{0.5}$ (43)			
Heat incident at aperture (W)	$\dot{Q}_{ap}$	157.27	9.79%

Parameter (units)	Symbol	Expanded uncertainty	Relative uncertainty
$$\delta(\dot{Q}_a) = \begin{bmatrix} (\eta_{ref} A_d I_{sun})^2 \times \delta^2(IF) \\ +(IF A_d I_{sun})^2 \times \delta^2(\eta_{ref}) \\ +(\eta_{ref} IF I_{sun})^2 \times \delta^2(A_d) \\ +(\eta_{ref} IF A_d)^2 \times \delta^2(I_{sun}) \end{bmatrix}^{0.5}$$ (44)			
First-law efficiency (receiver) (-)	η_{rec}	0.05	9.98%
$$\delta(\eta_{rec}) = \left[\left(\frac{1}{\dot{Q}_{ap}}\right)^2 \delta^2(\dot{Q}_i) + \left(-\frac{\dot{Q}_i}{\dot{Q}_{ap}^2}\right)^2 \delta^2(\dot{Q}_{ap})\right]^{0.5}$$ (45)			
Change in exergy (W)	$\Delta\Psi_w$	20.17	8.52%
$$\delta(\Psi_w) = \begin{bmatrix} ([(h_w - h_\infty) - T_\infty(s_w - s_\infty)])^2 \times \delta^2(\dot{m}_w) \\ +(\dot{m}_w)^2 \times \delta^2(h_w) \\ +(-\dot{m}_w)^2 \times \delta^2(h_\infty) \\ +(-\dot{m}_w(s_w - s_\infty))^2 \times \delta^2(T_\infty) \\ +(-T_\infty \dot{m}_w)^2 \times \delta^2(s_w) \\ +(T_\infty \dot{m}_w)^2 \times \delta^2(s_\infty) \end{bmatrix}^{0.5}$$ (46)			
Available work at aperture (W)	Φ_{ap}	157.27	9.79%
$$\delta(\Phi_{ap}) = \left[\left(1 - \frac{4T_\infty}{3T_{sun}}\right)^2 \delta^2(\dot{Q}_{ap}) + \left(-\frac{4\dot{Q}_{ap}}{3T_{sun}}\right)^2 \delta^2(T_\infty)\right]^{0.5}$$ (47)			
Second-law efficiency (-)	η_{2nd}	0.02	12.98%
$$\delta(\eta_{2nd}) = \begin{bmatrix} \left(\frac{1}{\Phi_{ap}}\right)^2 \times \delta^2(\Psi_{\text{out}}) \\ +\left(-\frac{1}{\Phi_{ap}}\right)^2 \times \delta^2(\Psi_{\text{in}}) \\ +\left(\frac{\Psi_{\text{out}} - \Psi_{\text{in}}}{\Phi_{ap}^2}\right)^2 \times \delta^2(\Phi_{ap}) \end{bmatrix}^{0.5}$$ (48)			

Nomenclature

Alphabetical

symbol	Description	Unit
A	Area	m^2
$\bar{A}$	Major axis length	m
$\bar{B}$	Minor axis length	m
b	Calibration variance	-
D	Diameter	m
F	View factor	-
Gr	Grashof number	-
h	Specific enthalpy	J/kg
$\bar{h}$	Convection heat transfer coefficient	$W/m^2.K$
I	Irradiance	W/m^2
$\bar{I}$	Irreversibility	W
IF	Intercept factor	-
k	Thermal conductivity	W/m.°C
L	Length	m
m	Mass	kg
$\dot{m}$	Mass flow rate	kg/s
Nu	Nusselt number	-
n	Experimental constant	-
P	Pressure	Pa
Pr	Prandtl number	-
$\dot{Q}$	Heat transfer rate	W
R	Thermal resistance	W/K
R^2	Correlation coefficient	-
Ra	Rayleigh number	-
Re	Reynolds number	-
s	Geometric constant	-
s	Specific entropy	J/kg.K
T	Temperature	°C
V	Average velocity	m/s
v	Kinematic viscosity	m^2/s
x	x-coordinate	m
x	Measured value	-
y	y-coordinate	m

Greek

symbol	Description	Unit
α	Absorptivity	-
β	Thermal expansion coefficient	1/K
ΔH	Change in enthalpy	J
ΔW	Change in work	W
$\Delta \Phi$	Change in available work	W
$\Delta \Psi$	Change in exergy	W
δ	Standard uncertainty	-
ε	Emissivity	W/m^2K^4

η	Efficiency	-
θ	Elevation angle	° (degrees)
μ	Dynamic viscosity	kg/m.s
ρ	Density	Kg/m^3
ρ	Reflectivity	-
σ	Stephan Boltzmann constant	W/m^2K^4
τ	Transmissivity	-
Φ	Available work	W
φ	Inclination angle	° (degrees)
Ψ	Exergy	W

Subscript

symbol	Description
$2nd$	Second law
∞	Ambient
abs	Absorbed
ap	Aperture
avg	Average
$back$	Back
$bottom$	Bottom
c	Characteristic parameter
$camera$	Camera
col	Collector
$combined$	Combined
$cond$	Conduction
$conv$	Convection
cp	CoolProp
$dish$	Dish
$emit$	Emitted
$excl$	Excluding
f	Film property
$forced$	Forced convection
$front$	Front
i	Inner wall
i	Increment
in	Control volume inlet
ins	Insulation
L	Characteristic length
LFM	Lunar flux mapping
$left$	Left
$loss$	Loss from control volume
$mylar$	Mylar facet
$natural$	Natural convection
net	Net
o	Outer wall
out	Control volume outlet
$prop$	Fluid property
rad	Radiation

rec	Receiver
ref	Reflectivity / reflected
ref	Reference
$right$	Right
s	Surface
$steel$	Steel
sun	Sun
th	Thermal efficiency
top	Top
$total$	Total
w	Working fluid (water)
$wind$	Wind

Acronym	Description
DAQ	Data acquisition device
DNI	Direct normal irradiance
EOS	Electro-optical System
IAPWS	International Association of Properties of Water and Steam
PV	Photovoltaic
TC	Thermocouple
TES	Thermal energy storage
UV-VIS	Ultraviolet and visible light

References

[1] International Energy Agency, "World energy outlook special report – Africa energy outlook," Paris, France, 2014.

[2] G. Legros, I. Havet, N. Bruce, and S. Bonjour, "The energy access situation in developing countries: A review focusing on the least developed countries and sub-Saharan Africa," New York, NY, United States, 2009.

[3] S. Baurzhan and G. P. Jenkins, "Off-grid solar PV: Is it an affordable or appropriate solution for rural electrification in sub-Saharan African countries?," *Renewable and Sustainable Energy Reviews,* vol. 60, pp. 1405–1418, 2016, doi: https://doi.org/10.1016/j.rser.2016.03.016.

[4] G. Knier. "How do photovoltaics work?" NASA Science. https://science.nasa.gov/science-news/science-at-nasa/2002/solarcells (accessed 15/03/2019.

[5] N. J. Jeon *et al.*, "Compositional engineering of perovskite materials for high-performance solar cells," *Nature,* vol. 517, no. 7535, pp. 476-480, 2015/01/01 2015, doi: 10.1038/nature14133.

[6] Y. M. Seshie, K. E. N'Tsoukpoe, P. Neveu, Y. Coulibaly, and Y. K. Azoumah, "Small scale concentrating solar plants for rural electrification," *Renewable and Sustainable Energy Reviews,* vol. 90, pp. 195-209, 2018.

[7] Y. W. Wong and K. Sumathy, "Solar thermal water pumping systems: a review," *Renewable and Sustainable Energy Reviews,* vol. 3, no. 2, pp. 185–217, 1999, doi: https://doi.org/10.1016/S1364-0321(98)00018-5.
[8] B. Ali, "Comparative assessment of the feasibility for solar irrigation pumps in Sudan," *Renewable and Sustainable Energy Reviews,* vol. 81, pp. 413–420, 2018, doi: https://doi.org/10.1016/j.rser.2017.08.008.
[9] S. Mohammed Wazed, B. R. Hughes, D. O'Connor, and J. Kaiser Calautit, "A review of sustainable solar irrigation systems for sub-Saharan Africa," *Renewable and Sustainable Energy Reviews,* vol. 81, pp. 1206–1225, 2018, doi: https://doi.org/10.1016/j.rser.2017.08.039.
[10] G. Alva, Y. Lin, and G. Fang, "An overview of thermal energy storage systems," *Energy,* vol. 144, pp. 341–378, 2018, doi: https://doi.org/10.1016/j.energy.2017.12.037.
[11] J. Paulides, E. Post, J. Post, L. Encica, and E. Lomonova, "Green turbine: A high speed double turbine solution for sustainable energy harvesting from waste heat," in *2015 Tenth International Conference on Ecological Vehicles and Renewable Energies (EVER)*, 2015: IEEE, pp. 1-7.
[12] J.-L. Bouvier, V. Lemort, G. Michaux, P. Salagnac, and T. Kientz, "Experimental study of an oil-free steam piston expander for micro-combined heat and power systems," *Applied Energy,* vol. 169, pp. 788-798, 2016/05/01/ 2016, doi: https://doi.org/10.1016/j.apenergy.2016.01.122.
[13] K. Mayer, "Research, development and demonstration of micro-CHP system for residential applications," Ecr International, Incorporated, 2010.
[14] P. Song, M. Wei, L. Shi, S. N. Danish, and C. Ma, "A review of scroll expanders for organic Rankine cycle systems," *Applied Thermal Engineering,* vol. 75, pp. 54-64, 2015/01/22/ 2015, doi: https://doi.org/10.1016/j.applthermaleng.2014.05.094.
[15] S. Pavlovic, E. Bellos, W. G. Le Roux, V. Stefanovic, and C. Tzivanidis, "Experimental investigation and parametric analysis of a solar thermal dish collector with spiral absorber," *Applied Thermal Engineering,* vol. 121, pp. 126-135, 2017, doi: https://doi.org/10.1016/j.applthermaleng.2017.04.068.
[16] O. Aboelwafa, S. E. K. Fateen, A. Soliman, and I. M. Ismail, "A review on solar Rankine cycles: Working fluids, applications, and cycle modifications," *Renewable and Sustainable Energy Reviews,* vol. 82, pp. 868–885, 2018, doi: https://doi.org/10.1016/j.rser.2017.09.097.
[17] A. Giovannelli, "State of the art on small-scale concentrated solar power plants," *Energy Procedia,* vol. 82, pp. 607–614, 2015, doi: https://doi.org/10.1016/j.egypro.2015.12.008.
[18] B. F. Tchanche, G. Papadakis, G. Lambrinos, and A. Frangoudakis, "Fluid selection for a low-temperature solar organic Rankine cycle," *Applied Thermal Engineering,* vol. 29, no. 11, pp. 2468–2476, 2009, doi: https://doi.org/10.1016/j.applthermaleng.2008.12.025.
[19] R. Loni, A. B. Kasaeian, E. Askari Asli-Ardeh, B. Ghobadian, and S. Gorjian, "Experimental and numerical study on dish concentrator with cubical and cylindrical cavity receivers using thermal oil," *Energy,* vol. 154, pp. 168–181, 2018, doi: https://doi.org/10.1016/j.energy.2018.04.102.
[20] R. Loni, A. B. Kasaeian, E. Askari Asli-Ardeh, and B. Ghobadian, "Optimizing the efficiency of a solar receiver with tubular cylindrical cavity for a solar-powered

organic Rankine cycle," *Energy,* vol. 112, pp. 1259–1272, 2016, doi: https://doi.org/10.1016/j.energy.2016.06.109.
[21] R. Loni, A. B. Kasaeian, E. Askari Asli-Ardeh, B. Ghobadian, and W. G. Le Roux, "Performance study of a solar-assisted organic Rankine cycle using a dish-mounted rectangular-cavity tubular solar receiver," *Applied Thermal Engineering,* vol. 108, pp. 1298–1309, 2016, doi: https://doi.org/10.1016/j.applthermaleng.2016.08.014.
[22] W. R. Dean, "XVI. Note on the motion of fluid in a curved pipe," *The London, Edinburgh, and Dublin Philosophical Magazine and Journal of Science,* vol. 4, no. 20, pp. 208–223, 1927, doi: 10.1080/14786440708564324.
[23] K. Ishida, "Two-phase flow with heat transfer in helically-coiled tubes," Empirical College, London, United Kingdom, 1981.
[24] W. Cui, L. Li, M. Xin, T. C. Jen, Q. Liao, and Q. Chen, "An experimental study of flow pattern and pressure drop for flow boiling inside microfinned helically coiled tube," *International Journal of Heat and Mass Transfer,* vol. 51, no. 1, pp. 169–175, 2008, doi: https://doi.org/10.1016/j.ijheatmasstransfer.2007.04.014.
[25] H. Zhu, Z. Li, X. Yang, G. Zhu, J. Tu, and S. Jiang, "Flow regime identification for upward two-phase flow in helically coiled tubes," *Chemical Engineering Journal,* vol. 308, pp. 606–618, 2017, doi: https://doi.org/10.1016/j.cej.2016.09.100.
[26] A. M. Fsadni and J. P. Whitty, "A review on the two-phase heat transfer characteristics in helically coiled tube heat exchangers," *International Journal of Heat and Mass Transfer,* vol. 95, pp. 551-565, 2016.
[27] C. Roosendaal, J. Swanepoel, and W. Le Roux, "Performance analysis of a novel solar concentrator using lunar flux mapping techniques," *Solar Energy,* vol. 206, pp. 200-215, 2020.
[28] G. Zanganeh, R. Bader, A. Pedretti, M. Pedretti, and A. Steinfeld, "A solar dish concentrator based on ellipsoidal polyester membrane facets," *Solar Energy,* vol. 86, no. 1, pp. 40–47, 2012, doi: https://doi.org/10.1016/j.solener.2011.09.001.
[29] A. Giostri and E. Macchi, "An advanced solution to boost sun-to-electricity efficiency of parabolic dish," *Solar Energy,* vol. 139, pp. 337–354, 2016, doi: https://doi.org/10.1016/j.solener.2016.10.001.
[30] W. Reinalter *et al.*, "Detailed performance analysis of a 10kW dish/Stirling system," *Journal of Solar Energy Engineering,* vol. 130, no. 1, p. 011013, 2007, doi: 10.1115/1.2807191.
[31] W. B. Stine and R. W. Harrigan, "Solar energy fundamentals and design : With computer applications," in *Alternate energy*. New York, NY, United States: Wiley, 1985, pp. 0735–8210.
[32] W. B. Stine and G. G. McDonald, "Cavity receiver convection heat loss," in *Proceedings of the International Solar Energy Society – Solar World Congress (SWC)*, Japan, 1989, vol. 1318.
[33] Agilent. "Cary 100 UV-Vis." https://www.agilent.com (accessed 23/06/2019.
[34] M. J. Brooks *et al.*, "SAURAN: A new resource for solar radiometric data in Southern Africa," *Journal of Energy in Southern Africa,* vol. 26, no. 1, pp. 2–10, 2015.
[35] N. Geuder, S. Wilbert, and N. Janotte, "Precise measurements of solar beam irradiance through improved sensor calibration," in *Proceedings of SolarPACES 2009*, Berlin, Germany, 2009, pp. 1–8.
[36] S. O. Onyegegbu and J. Morhenne, "Transient multidimensional second law analysis of solar collectors subjected to time-varying insolation with diffuse components,"

Solar Energy, vol. 50, no. 1, pp. 85–95, 1993, doi: https://doi.org/10.1016/0038-092X(93)90010-L.

[37] W. G. Le Roux, T. Bello-Ochende, and J. P. Meyer, "A review on the thermodynamic optimisation and modelling of the solar thermal Brayton cycle," *Renewable and Sustainable Energy Reviews,* vol. 28, pp. 677–690, 2013, doi: https://doi.org/10.1016/j.rser.2013.08.053.

[38] R. Y. Ma, "Wind effects on convective heat loss from a cavity receiver for a parabolic concentrating solar collector," Sandia National Laboratories, Albuqerque, NM, United States, SAND-92-7293, 1993.

[39] M. Uzair, "Wind induced heat losses from solar dish-receiver systems," Auckland University of Technology, Auskland, New Zealand, 2018.

[40] K. S. Reddy, G. Veershetty, and T. S. Vikram, "Effect of wind speed and direction on convective heat losses from solar parabolic dish modified cavity receiver," *Solar Energy,* vol. 131, pp. 183–198, 2016.

[41] K. S. Reddy, T. S. Vikram, and G. Veershetty, "Combined heat loss analysis of solar parabolic dish – modified cavity receiver for superheated steam generation," *Solar Energy,* vol. 121, pp. 78–93, 2015, doi: https://doi.org/10.1016/j.solener.2015.04.028.

[42] J. A. Harris and T. G. Lenz, "Thermal performance of solar concentrator/cavity receiver systems," *Solar Energy,* vol. 34, no. 2, pp. 135–142, 1985, doi: https://doi.org/10.1016/0038-092X(85)90170-7.

[43] Y. A. Cengel and A. J. Ghajar, *Heat and mass transfer: Fundamentals and applications*, 5th ed. New York, NY, United States: McGraw-Hill Education, 2014.

[44] A. Žukauskas, "Heat transfer from tubes in crossflow," in *Advances in Heat Transfer*, vol. 8, J. P. Hartnett and T. F. Irvine Eds. New York, NY, United States: Academic Press, 1972, pp. 93–160.

[45] T. Fujii and H. Imura, "Natural-convection heat transfer from a plate with arbitrary inclination," *International Journal of Heat and Mass Transfer,* vol. 15, no. 4, pp. 755–767, 1972, doi: https://doi.org/10.1016/0017-9310(72)90118-4.

[46] G. C. Vliet, "Natural convection local heat transfer on constant-heat-flux inclined surfaces," *Journal of Heat Transfer,* vol. 91, no. 4, pp. 511–516, 1969, doi: 10.1115/1.3580235.

[47] Firebird Thermal Products. "Ceramic fibre products." http://www.firebirdref.com/a/caipin/toupan/ (accessed 23/04/2019.

[48] M. Padki, H. Liu, and S. Kakac, "Two-phase flow pressure-drop type and thermal oscillations," *International journal of heat and fluid flow,* vol. 12, no. 3, pp. 240-248, 1991.

[49] L.-J. Guo, Z.-P. Feng, and X.-j. Chen, "Transient convective heat transfer of steam–water two-phase flow in a helical tube under pressure drop type oscillations," *International journal of heat and mass transfer,* vol. 45, no. 3, pp. 533-542, 2002.

[50] L.-J. Guo, Z.-P. Feng, and X.-J. Chen, "Pressure drop oscillation of steam–water two-phase flow in a helically coiled tube," *International Journal of Heat and Mass Transfer,* vol. 44, no. 8, pp. 1555-1564, 2001/04/01/ 2001, doi: https://doi.org/10.1016/S0017-9310(00)00211-8.

[51] L. Santini, A. Cioncolini, C. Lombardi, and M. Ricotti, "Dryout occurrence in a helically coiled steam generator for nuclear power application," in *EPJ Web of Conferences*, 2014, vol. 67: EDP Sciences, p. 02102.

[52] W. Zhao *et al.*, "Thermal Energy Storage Using Zinc as Encapsulated Phase Change Material," in *ASME 2011 International Mechanical Engineering Congress and Exposition*, 2011, vol. Volume 4: Energy Systems Analysis, Thermodynamics and Sustainability; Combustion Science and Engineering; Nanoengineering for Energy, Parts A and B, pp. 849-856, doi: 10.1115/imece2011-63988. [Online]. Available: https://doi.org/10.1115/IMECE2011-63988

[53] J. Q. Sun, R. Y. Zhang, Z. P. Liu, and G. H. Lu, "Thermal reliability test of Al–34%Mg–6%Zn alloy as latent heat storage material and corrosion of metal with respect to thermal cycling," *Energy Conversion and Management,* vol. 48, no. 2, pp. 619-624, 2007/02/01/ 2007, doi: https://doi.org/10.1016/j.enconman.2006.05.017.

[54] J. Zhu *et al.*, "Experimental study of the energy and exergy performance for a pressurized volumetric solar receiver," *Applied Thermal Engineering,* vol. 104, pp. 212-221, 2016.

[55] V. C. Sharma and A. Sharma, "Solar properties of some building elements," *Energy,* vol. 14, no. 12, pp. 805–810, 1989, doi: https://doi.org/10.1016/0360-5442(89)90034-0.

[56] ISO/IEC Guide 98-3:2008, "Uncertainty of measurement – Part 3: Guide to the expression of uncertainty in measurement (GUM:1995)," ISO/IEC, Geneva, Switzerland, 2008.

[57] C. K. Ho and S. S. Khalsa, "A photographic flux mapping method for concentrating solar collectors and receivers," *Journal of Solar Energy Engineering,* vol. 134, no. 4, p. 041004, 2012, doi: 10.1115/1.4006892.

[58] G. Burgess, J. Zapata, R. Chauvin, M. Shortis, J. Pye, and J. Preston, "Three-dimensional flux prediction for a dish concentrator cavity receiver," in *Proceedings of SolarPACES 2012*, Marrakech, Morocco, 2012.